UNIVERSIDAD DE CONCEPCIÓN

KINEMATICS IN THE INNER KPC OF THE SEYFERT GALAXY UGC 2024

(CINEMÁTICA EN EL KPC CENTRAL DE LA GALAXIA SEYFERT UGC 2024)

TESIS PARA OPTAR AL GRADO DE MAGÍSTER EN CIENCIAS CON MENCIÓN EN FÍSICA

DANIA BELÉN MUÑOZ VERGARA

TUTOR: DR. NEIL NAGAR

CONCEPCIÓN, CHILE
DICIEMBRE 2017

Agradecimientos

Así como las estrellas son incontables, es incontable la cantidad de personas a las que quiero agradecer en este momento. Intentaré mencionar a la mayoría. A Lorena, Esaú, Sebastián, Fabián y Daniela, uds. han sido el cable a tierra en este viaje al Universo. A Agustín e Isabel, uds. son los amores, la paz y las alegrías de mi vida. A mis abuelitos, los que aún están conmigo compartiendo esta experiencia y los que me han acompañado todos estos años desde donde sea que el fin de la vida los haya llevado. Gracias a mi familia por las reuniones, las risas y las bromas, que me ayudaron tanto a mantener mi mente sana durante este tiempo. Debo hacer una mención especial a mi tío Pato, un millón de gracias por permitirme vivir en su casa y aguantar mis peores humores universitarios.
También quiero agradecer a todos mis amigos, que de una u otra forma fueron parte de esta aventura. A Andreita, es infinito el agradecimiento que tengo hacia ti y tu familia, porque desde antes de la Astronomía que uds. me han apoyado y querido como si fuera una más; Pame, conocerte y a tu familia fue un regalo de la vida, nunca podré expresar completamente lo agradecida que estoy por haberme abierto las puertas de su hogar en cualquier ocasión y por tratarme como si hubiese sido parte de sus vidas desde siempre. Diego, gracias por la compañía, los abrazos, las comidas, las conversaciones, por pensar siempre que podía y decirme con convicción que así era, simplemente, gracias por todo.
No puedo terminar sin antes mencionar a las personas especiales del dpto. de Astronomía. A mis compañeros de oficina, los originales: Carla, Valeria, Aldo, Camila, Mauro, Nelvy, Alejandra, Heinz y Fernando (Bodoque) y a la nueva camada: Coté, Joshe, Pedro y Matus.

Abstract

Understanding how mass is transferred from galactic scales down to nuclear scales to feed the central supermassive black hole (hereafter SMBH) has been a long-standing problem in the study of nuclear activity in galaxies given that it is widely accepted that the prodigious energy emitted by the active galactic nucleus (AGN) is a result of accretion into the SMBH, which implies the presence of a gas reservoir close to the AGN.

This thesis presents the study of one more AGN hosting galaxy, which is going to increase the sample of object studied to understand feeding and feedback processes between the galaxy and its nucleus. The galaxy studied was UGC 2024, which is a Sab galaxy (in the Hubble diagram) hosting a Seyfert 2 nucleus. This kind of nuclei are characterized by the presence of Narrow Line Regions (NLR), this meas, they only present emission line widths of less than 500 km s^{-1}.

Studying the NLR of AGN's have being a key instrument to the understanding of the causes of the perturbations present in the centre of active galaxies. Nowadays specialist instruments in observatories are available that allows to better reproduce the galaxy behaves by observing spectra of almost every 0.1 arcsecond in the object with a high spectral resolution. In this study the GEMINI Multi-Object Spectrograph (GMOS) was used to unravel the features of the inner 3.44×4.84 arcsec^2 of UGC 2024, revealing an outflow with a wide open angle and a mass of $\sim 1 \times 10^6 M_\odot$ and perturbations that can be associated to a bar in the kinematics of the ionized gas.

Resumen

Entender cómo la masa es transferida desde escalas galácticas hasta nucleares para alimentar el agujero negro supermasivo (SMBH por su acrónimo en inglés) central ha sido un problema duradero en el estudio de la actividad nuclear en las galaxias dado que es largamente aceptado que la enorme cantidad de energía emitida por el Nucleo Activo de Galaxia (AGN, por su acrónimo en inglés) es un resultdo de la acreción dentro del SMBH, lo que implica la presencia de una reserva de gas cercana al AGN.

Esta tesis presenta el estudio de una galaxia que contiene un AGN, la cual incrementará la muestra de objetos estudiados apra entender los procesos de alimentación y retroalimentación entre la galaxia y su núcleo. The galaxia estudiada fue UGC 2024, que es una galaxia Sab (en el diagrama de Hubble) conteniendo un núcleo Seyfert 2. Este tipo de núcleos están caracterizados por la presencia de Regiones de Línea Delgada (NLR, por si acrónimo en inglés), lo que significa que sólo posee anchos en las líneas de emisión de menos de 500 km s^{-1}.

Estudiar la NLR de los AGN's ha sido un instrumento clave para el entendimiento de las causas de las perturbaciones presentes en el centro de las galaxias activas. Hoy en día hay instrumentos especializados en los observatorios que permiten una mejor reproducción de los comportamientos de las galaxias a través de la observación de los espectros de al menos cada 0.1 arco segundo en el objeto con una alta resolución espectral. En este estudio el Espectrógrafo de Multi-Objetos de GEMINI (GMOS, por su acrónimo en inglés) fue utilizado para desentrañar las características de los 3.44×4.84 arcsoegundos^2 más internos de UGC 2024, revelando gas saliente (outflow) con un ángulo de apertura ancho y una masa de $\sim 1 \times 10^6 M_\odot$ y perturbaciones que pueden ser asociadas a una barra en la cinemática del gas ionizado.

Contents

List of Figures

List of Tables

Chapter 1

Introduction

1.1 Active Galactic Nuclei (AGN).

The term AGN refers to the presence of energetic phenomena in the nucleus of galaxies when it cannot be related directly with stars. This objects present a wide observational properties, which can be used to identify them in surveys using a range of selection techniques and most of them are based on the properties the galactic nuclei has at a given wavelength region, that says, selection methods are incomplete for some AGNs luminosities, classes or redshifts [15].

The typical anatomy of an AGN can be seen in figure 1.1 . Here is possible to observe the Accretion Disk, which is hot and has luminous gas accreting onto the Black Hole. The Jet is formed by charged particles moving with a relativistic velocities out of the nucleus. There are a Broad-line Region and a Narrow-line Region (hereafter BLR & NLR respectively), the BLR consist in clouds of gas near the accretion disk and presents turbulent motion at high speed, while the NLR is formed by gas clouds further out moving with slower speed. The Obscuring Torus is a ring of gas and dust surrounding the central black hole [1].

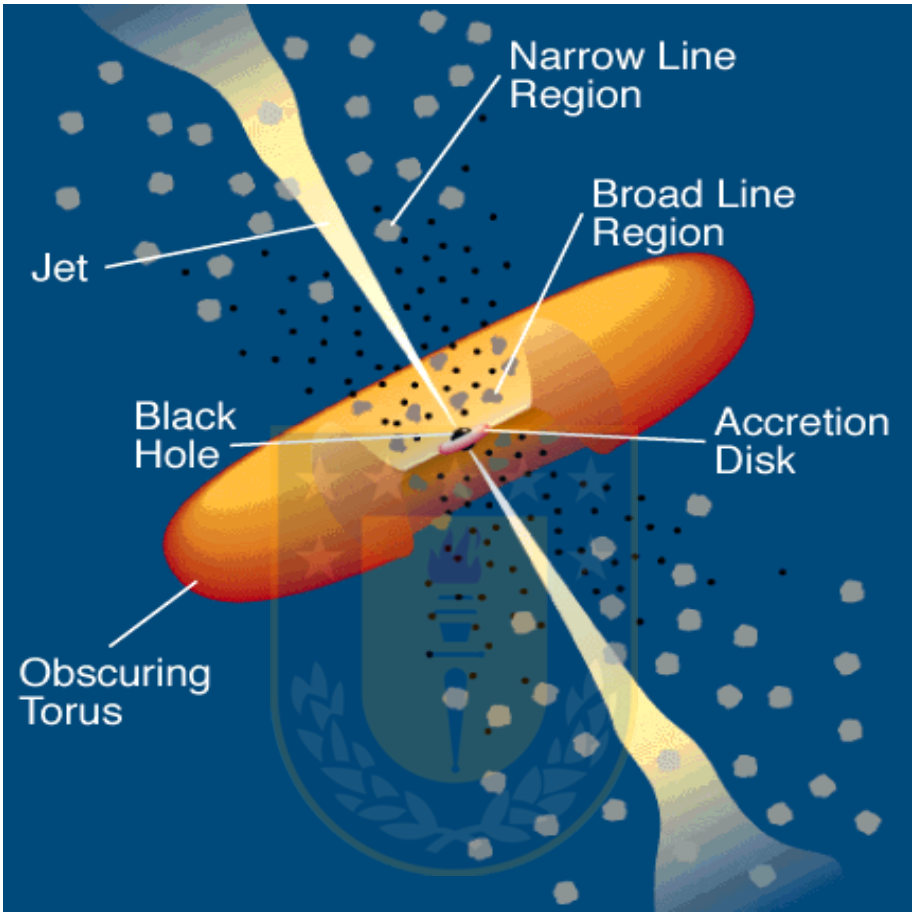

Figure 1.1: Urry and Padovani Model for Radio-Loud AGN. (Credit: C.M. Urry and P. Padovani [79])

1.2 Unified Model.

If the observation is made from the "down" area, it corresponds to a Radio Quiet QSO, while from the "up" area a Radio Loud QSO is observed. Seyfert 1 are those observed directly to the accretion disk and Seyfert 2 are observed from the obscuring torus, as is shown in figure 1.2.

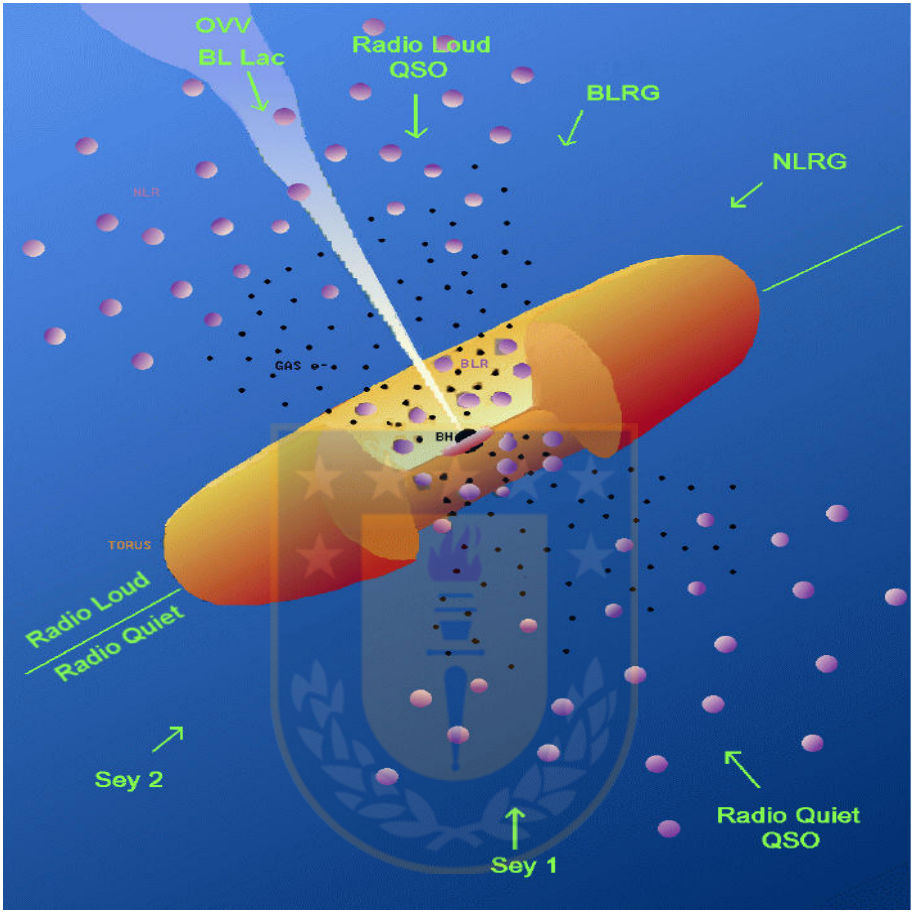

Figure 1.2: Line of sight for different AGN definitions according to the unified model based on the original figure of [79]. (Credit: The Essential Radio Astronomy course at NRAO)

It is still a mystery how is the exactly way of the feeding of an AGN, but we can say this happen due to the accretion of gas towards a Super Massive Black Hole (SMBH). We can divide this whole group in two smaller groups:Quasars and Seyfert Galaxies, being the last group the commonest in the Universe.

The name Quasar comes from "Quasi Stellar Radio Source". "Quasi Stellar" because their appearance did not suggest a relation with galaxies at the

beginning due to the great distance between they and us, so what we see is a star-like nuclear source and since the surrounding galaxy has a small angular size and it is faint, it is lost in the glare of the nucleus. If the observation is made from the "down" area, it corresponds to a Radio Quiet QSO, while from the "up" area a Radio Loud QSO is observed. In a typical quasars the luminosity of the nuclear source is brighter than the luminosity of the stars in the host galaxy by a factor of 100. These objects were initially discovered in the late 1950s as a result of the first radio surveys of the sky (3C and 3CR Catalogs, PKS, 4C Catalog, et al.). The main characteristics of quasars are: they are star-like objects identified with radio sources, large redshifts, large UV flux, time-variable continuum flux, broad emission lines [3].

The first spectrum of a Seyfert was obtained at Lick Observatory 1908 by E. A. Fath. But was Carl Seyfert [69] the first in realize that there are similar galaxies which form a different class. He found important characteristics on the spectra of some galaxies (NGC1068, NGC1275, NGC3516, NGC4051, NGC4151, and NGC7469): 1)The lines are broad and 2)Hydrogen lines are broader than other lines in some cases [69]. In 1959 Woltjer try to understand for the first time the physics of Seyfert galaxies finding: 1)The nuclei is unresolved, so the size of this is less than 100 parsec (pc), 2)The nuclear emission may last at least 10^8 years, because Seyfert galaxies represent about 0.001% of spiral galaxies and 3) If the material in the nucleus is gravitationally bound, then the mass of the nucleus has to be very high [86]. Seyfert galaxies are divided as Seyfert 1 and Seyfert 2 depending on their spectrum. This classification was possible thanks to the optical region in which appear permitted and forbidden emission lines. In the first one the hydrogen lines are broader than the forbidden lines, instead in Seyfert 2 galaxies the hydrogen lines has the same width as the forbidden lines. Lately, Osterbrock published new intermediate classifications: Seyfert 1.5 y Seyfert 1.8 y 1.9 [48], related to the width and intensity of the permitted and forbidden lines. At the beginning, the classification was only descriptive but later it took a more astrophysical meaning: the permitted lines can appear in very much denser regions than the forbidden lines, these dense regions are reflected only in the BLR, which are present in Seyfert 1 galaxies uniquely. I mentioned before, the velocity of the gas cloud in BLR is very high due the nearness with the nucleus, it could cause the great width in permitted lines. On the contrary, the NLR, in which are formed permitted and forbidden lines, moves with lower velocity, cause it

is located further out. Specifically, Seyfert 2 Galaxies present an excess dust emission in the optical continuum [1], it is because we observed its nucleus through the torus equator (edge-on) and then, we only detect the Narrow Line Region (NLR) [68].

The Unified Model suggests the division of Seyfert 1 and Seyfert 2 galaxies is a matter of orientation([1], [6], [80]). According to this model the accretion disc of the AGN is surrounding by a torus of dust and molecular gas geometrically and optically thick, where the X-ray and UV radiation are reprocessed and remitted as Mid infrared radiation [54], i.e., both Seyfert 1 and Seyfert 2 galaxies would be the same object observed in different orientations of the accretion disc.

1.3 Galaxy Kinematics in Nearby AGNs.

Since the distribution of the gas bear on the radial velocity measurements I will discuss it briefly. Observations in the optical emission lines require ionized gas (in HII regions or in tenuous areas between them). The surface number-densities of HII regions change with the radius, it is small in the central areas of intermediate and later-type galaxies, increase to a maximum and then decrease to small values near the optical boundaries [34]. The low efficiency of HII regions in the central part of the galaxies is usually correlated with the decrease of the HI surface density in these area
citepDAVIES72. The above supports that star formation is less potent in regions of lower gas density [83]. The accelerated reduction of the gas by star formation may be the cause of the central depression [71, 83]. For a great number of spiral galaxies of large angular size the angular resolution of the radio HI synthesis map is sufficient to separate spiral arms from each other. In some of this galaxies (M31, M33, M51, et al.) the HI distribution shows spiral structure associated with the optical morphology in a general way [83]. Precisely calibrated maps of the distribution and motions of the ionized gas of spiral galaxies would give the basis for quantitative comparison with radio-synthesis observations [83].

We can say that galaxies of all type show rotation (In general, the pattern of the velocity fields is always dominated by rotation), even if they are irregular,elliptical or spiral galaxies. The observed velocity fields show more frequently that exist deviation from the symmetry expected for purely circular

motion and that these deviation can be large. We interpreted deviations as bars and oval distortions, wraps, density wave and nuclear explosions. The pattern of circular motion usually prevail on the velocity fields determined by optical emission lines and radio-HI data, this apply to the gas and also the motion of the stars is represented by the same general kinematics, e.g., in the central region of M31 the stars exhibit a velocity field as complex as that of the gas [61], and the information on the rotation of the stars is obtained from the optical absorption lines and restricted to the central regions. Besides the regular rotation, local noncircular motions in the stars have been reported by Simkin [72] and these seem to be associated with dust patches and other details of the spiral structure.

The observation of the redshift and blueshift let us determine the velocity distribution of the galaxy in the line of sight and then is possible to build the radial velocity field.

Determination of the velocity field over the entire disk of a galaxy would provide important additional information, the amount and extent of the noncircular motions would be more clearly revealed and the orientation of the parameters could be determined directly from the velocity field and not from the distribution of broad-band light over the galaxy [83]. It is well known that neutral hydrogen gas in late type galaxies extend to large radii, so mapping the HI velocity field would provide independent and complementary information on the kinematics but there is an important limitation with radio-HI observations, many intermediate-type galaxies have little HI in central regions, so the velocity field of central regions in many galaxies can be better measured by optical means.

The measurement of the radial velocity does not allow just one interpretation of the velocity field. To derive the rotational curve from the velocity field are necessary two assumptions: 1) we measure all the data of the galaxy in a inclined plane with coordinates R (Radio measured from the galactic center) and θ (azimuth angle) and usually the motion trough the z axis is not considered; 2) rotation is dominant and all noncircular motions are not part of a large-scale pattern [83]. It is usual to use numerical schemes to determine important parameters: Position angle (PA) of the line of nodes, coordinates of the rotation center, systemic velocity V_{sys} and the inclination i of the normal to the galaxy plane with the line of sight. A small error in these parameters can

result in patterns with characteristics symmetries in the diagram of the radial velocity field after subtraction of the nominal rotation curve, which was first illustrated by [84] (1.3) in their study of M33. This subtraction is important when we want to study the noncircular motion, because is important to establish what kind of motion can be found in the analysis and what kind will be hidden because they simulate the radial velocity field effects produced by an error in the dynamical parameters [84].

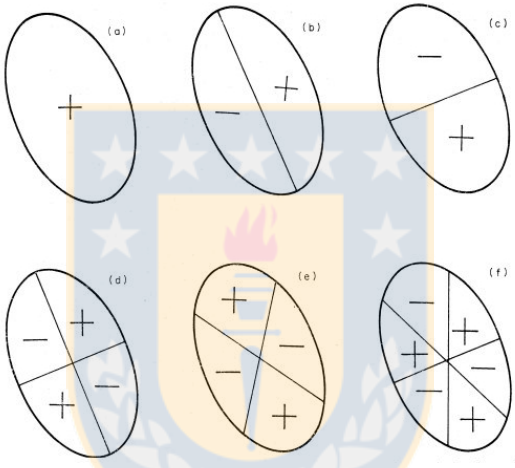

Figure 1.3: Model residual radial velocity field corresponding to small changes in the dynamical parameters: (a) V_{sys}; (b) PA; (c) Rotation curve; (d) Position of the rotation center (movement along minor axis); (e) Position of the rotation center (movement along major axis); (f) Inclination angle.(Credit: Warner et al. 1973 [84])

Figure 1.3 shows how can vary the residual of the radial velocity field with small changes in one parameter. The symmetries in the figure shows that the parameters are independent. [84] suggest that a good fit is obtained fixing one parameter at a value differing from the true one and varying the others. They present two types of non-circular motion that will be hard to detect:
a Expansion and contraction: the radial velocity field associated with expansion is similar to the associated with changes in the PA. The second gives a radial velocity proportional to the radius while the expansion or contraction

could be restricted to particular radial distances.
b Motion of the galaxy transverse to the line of sight: this is similar to solid body rotation of the galaxy about an axis perpendicular to the direction of transverse motion. The component in the direction of the minor axis gives a radial velocity field very similar to that in figure 1.3, associated to changes in the PA. The component in the direction of the major axis gives a solid body rotation in the plane of the disk. So the entire transverse motion would be incorporated to changes in PA and in the rotation curve.

1.4 Rotation Curve.

Was Pease in 1916 and 1918 [51, 52] who measured for the first time what we call "rotation curve" in the nuclear regions of M31 and The Sombrero Galaxy (M104). These observation required a lot of dedication, both exposure lasted 80 hours. That was the beginning of the study of rotation curves and since that moment it has matured to become in the most powerful tool for determining mass distribution inside galaxies, not in the inner regions but in the outer [24].

For a detailed comparison between radio curves and galaxy morphology is necessary to have observational results spanning the range of types and the range of luminosities within each type. From rotation curves measured over a large part of the optical disks of some galaxies, Roberts & Rots [58] suggest that the mass distribution of Sa galaxies were more centrally condensed than those of the Sc galaxies.

Measurements of the HI-21cm line velocities in galaxies let us assume that at large radii the rotation curve became Keplerian. In fact rotation curves are found to decline much more slowly or even not at all ([59], [36], [83].

As it was mentioned before, the necessary angular resolution in the central regions of galaxies is better from optical observations. Like example, the gas motions within about 0.4 kpc of the nucleus of M31 show a complex velocity field superposed on rapid rotation [60] with evidence for expansion at velocities up to 100 km s^{-1}. Observations of the interstellar K and H absorption lines indicate gas ejection from the nucleus with velocities up to 450 km s^{-1} [45]. Gas motions within 300 pc in M81 show outflows, but just outside this radius the velocity field shows a general inflow towards the center citepGOAD741,GOAD742. In the late 1970's, M31 as well as M81 were im-

portant to understand the behavior of the central regions of galaxies because they present nuclear activity and gas ejection on relatively small scale and the stamllerrs on the disk and the bulge of M31 do not seem to follow the pattern of noncircular motions seen in the gas [53].

The kinematics of the inner rings of HII regions, present in most galaxies, has been studied several times, i. e., the ring at ≈340 pc from the nucleus of NGC 3351 (an SBb galaxy) was studies by [62] and it is apparently contracting; [29] observed noncircular motion in the inner HII ring of HII regions in NGC 5364; NGC 4736 was studied by [81, 82], besides the HII regions its ring contains diffuse Hα emission with a sharp outer boundary at a radius of 1kpc, where a decrease of the in the optical continuum surface brightness and an increase in $B-V$ color is found. The HII kinematics studied by [81, 82] shows that expansion motions exist in the ring and the expansion is strongest at the position of the radio continuum peaks. Even if an explanation in terms of the inner Lindblad resonance seemed attractive, the direction of the noncircular motions does not appear to agree with that expected in the linear approximation.

[22] and also [77] present observations indicating outflows of gas from the nucleus if the NGC 253 into a cone-shaped region with velocities reaching 300 km s^{-1}.

So until 1978 there was good evidence in the velocity patterns of central regions of noncircular motions and even ejection of gas on the 1kpc scale and also there was evidence that stars are not appreciable affected by all the goings-on [83].

[56] present the kinematics in the inner pc of Mkr 1066, they found that the velocity field is dominated by rotation in the galaxy plane but shows an S-shape distortion along the galaxy minor axis which seems to be due to an oval structure seen in an optical continuum image. Along the oval they found a partial ring of low velocity dispersion attributed to intermediate-age stellar population. The velocity fields of all emission lines are dominated by a similar rotation patter to that observed for the stars, but are deformed by the presence of two structures: *a* a compact rotating disc with radius r≈ 70 pc; *b* a bi-conical outflow along the radio jet which is oriented approximately along the galaxy major axis. [16] observed nuclear gas spiral in the radio-galaxy Arp 102B, which indicates gas inflow towards the nucleus, four years later [17] present the same galaxy as a low-ionization nuclear emission-line region

(LINER)/Seyfert1, here the centroid velocity maps suggest that most gas is in rotation in an inclined disc with line of nodes along position angle $\approx$ 88deg, redshifts to the west and blueshifts to the east, with lower blueshifts correlated with the eastern arm and radio jet. This correlation suggests that the jet is interacting with gas in the disc. Also channel maps show blueshifts but also some redshifts at the eastern arm and jet location which can be interpreted as originated in the front and back walls of an outflow pushed by the radio jet.
[46, 68] they present the kinematics of the Seyfert 2 galaxy NGC 2110, Here the cold gas kinematics suggests that exist inflowing gas to the east and SW of the nucleus. NGC7213 [67] presents inflows towards the nucleus in the NW and SE regions and an increase in the gas velocity dispersion near the borders of the spiral arms.

1.5 About the Outflows and Inflows.

Galactic inflow and outflow are important due to their influence in the budget of baryon and star formation activities in galaxies and also play a role in their formation and evolution. In a grand picture of galaxy formation and evolution provided by ΛCDM cosmology, baryonic inflow into a galactic disk occurs when gas accretes from the intergalactic medium into the dark matter halo and subsequently collapses toward its central region [76]. Semi-analytic models, in which the most of the gas are assume to accrete into the galactic disk, predict that the slope of the galaxy luminosity function is much abrupt than that actually observed, i.e., according to the simulations, the gas cooling and accretion into the disk should be suppressed by feedback processes (e.g, UV radiation, supernovae explosions and active galactic nuclei). In summary, galactic outflow is driven by the feedback process and it has been observed all over in starburst galaxies at both high and low redshifts.
The stellar mass-metallicity relation shows that at each redshift there is an empirical upper limit for metallicity for massive galaxies, this implies that the chemical evolution in galaxies with this relation accompanies gas inflow and outflow processes.
[73] reports some results on the kinematics of the inner few hundred parsec (pc) around nearby AGN using optical and near-Infrared (NIR) integral field spectroscopy. The stellar kinematics of the hosts galaxies is dominated by

circular rotation in the plane of the galaxy. In the optical,inflow with velocities of $\sim$50 kms^{-1} had been observed along the nuclear spiral arms, whereas in the NIR these inflows had been observed in ionized gas emission for low-luminosity AGN and molecular gas emission for higher-luminosity AGN. Outflows had been observed in ionized gas emission from the NLR. Mass outflow rates in ionized gas range from 10^{-2} to 10^{-3} $M_{\odot}$ yr^{-1} and are 10–100 times larger than the mass accretion rates on to the AGN, supporting an origin for the bulk of the outflow in gas from the galaxy plane entrained by a nuclear jet or accretion disk wind. These outflows are a consequence of mass accretion on to the SMBH and they are characterized for be ubiquitous (ever-present) among AGN. On the other hand, inflows are infrequently observed.

It is common to observe nuclear spirals around AGN. [43] suggest that they are not self-gravitating and may be the channels through which matter is being transferred to the nucleus to feed the AGN. Gas kinematics of NGC 1097 and NGC 6951 were mapped using optical spectra. The fitting of the N[II]λ6584Åand Hα has allowed to find that the kinematics in the plane of NGC 1097 is dominated by rotation, but with noncircular motions superimposed. After isolate and spatially correlate the noncircular motion velocity field with a nuclear spiral structure, the suggestion that nuclear spiral indeed associated with inflows towards the nucleus was supported [20, 55]. For NGC 6951 [74] found similar results. The streaming motions along the nuclear spirals have velocities of $\approx$ 50 km s^{-1}, and the estimated mass inflow rate in ionized gas is $\approx 10^{-3} M\odot$ yr^{-1}, rate that coincide with the order of the mass accretion rate to the active nucleus ([73]).

Now, outflows in the optical were observed in several galaxies, e. g., NGC 2273, NGC 4051, NGC 1068, NGC 2110 and others more [18, 39, 41, 68, 87]. The stellar kinematics is dominated by rotation in the plane of the galaxy. The gaseous kinematics shows gas rotating in the plane of the stars. Furthermore,the gas kinematics in NGC 2273, NGC 4051 and NGC 3516 shows blueshift and redshift due to outflows from the nucleus. The outflows are spatially associated with the radio structure and both the radio flux maps and the [SIII] flux and centroid velocity maps show discrete components (knots of emission), which we interpret as due to intermittent ejection of plasma that compresses the surrounding interstellar medium, driving the observed outflows. This interpretation is supported by the observation of an increase in the gas velocity dispersion in the regions surrounding the radio knots [73]. If

channel maps along S[III] emission line were built, they would show that the highest velocities are found close to the nucleus (component originating in the galactic disk is the brightest near the nucleus), opposite to what is observed in the centroid velocity maps because in them the highest velocities are observed away from the nucleus(outflowing component is the brightest in this region). In the channel maps is possible to observe high velocity gas in the nucleus, i.e., the outflow does not leave the nucleus at 0 km s^{-1}.
NGC 2110 is a case where the radio jet is not well aligned with the ionized gas emission and main outflow [46].[7] lists some common properties among outflows in nearby AGN:

- NLR outflows, typically extending for a few hundred of parsecs, are found in all AGNs, with velocities ranging from $\approx$ 100 to 800 km s^{-1}.
- Mass outflow rates in the emitting gas range from 0.5 to 10 $M_{\odot}$ yr $^{-1}$, which are 100–1000 times the accretion rate which powers the AGN. This means that the outflow is a result of mass loading of a nuclear wind as it travels out through the interstellar medium of the galaxy.
- The filling factor of the emitting gas was estimated to be on the order of 10% in those galaxies for which such as estimate was possible.
- The typical power of the outflow is only of the order of 10^{-3} L_{bol}, but that is usually enough to expel from the nuclear region 10^7 - 10^8 M⊙ of gas in $\approx 10^7$ yr.
- The outflows usually follow the orientation of the radio jets, but in a few nearby objects they are not completely aligned (e.g., NGC1068, NGC 4151, NGC 2110). This mis-alignment implies a distinct orientation or warping between the inner funnel of the accretion disk, where the radio jet originates, and the more external region from which the wind that drives the ionized gas outflow originates.
- Recent modeling of the outflows in NGC 4151 and NGC 1068 indicate that the data does not require acceleration along the NLR, as suggested by previous studies.

The astronomical community was interested in two cases where inflows occur in the early 1990's: 1 bar-driven inflows in barred spiral galaxies can

lead to gas accumulation and star formation in nuclear rings of "hot spots" and 2 tidal interactions and mergers between galaxies can cause large amounts of gas to fall rapidly into their nuclei and produce luminous starburst and non-thermal activity [40]. Also velocity-resolved reverberation mapping suggests that the BLRs of AGNs can have significant net inflow [26].

Even though observe gas inflows is difficult directly, because they could be masked by more evident outflows, they are commonly predicted by numerical simulations of barred and interactive galaxies. The success of these simulations in matching many properties of such systems leaves a little doubt that inflows occur generally any time a non-axisymmetric gravitational potential is present. The fact that in many of the most luminous systems an amount of molecular gas comparable to the gas content of an entire large spiral galaxy is observed to be concentrated into a small nuclear region only a few hundred parsecs across is the evidence that gas inflows regions of galactic size are responsible for triggering the most energetic outbursts of activity in galactic nuclei.

Understand how gas condenses into galactic nuclei is important to understand the evolution of galaxies and of the universe because the major consequences of starburst and non-thermal activity on galactic nuclei are that star formation and the growth of the black hole can build up the central region of the galaxy and that the energy freed can heat and expel residual gas into an intergalactic medium [40].

Spiral patterns and bar-like distortions effect can be gas inflows in galaxies [40, 83]. Bars can be understand as a strong and open type of spiral pattern and in galaxies which present bars the departure of the gas motions from circular orbits can become very large, and can cause strong shocks to form along the leading edge of the bar, resulting in rapid energy dissipation and hence a strong inflow. These effect had been demonstrated in numerical simulations and in observations. Also it had been demonstrated that the gas tends to form rings with a double-peaked density distribution near the Inner Lindblad Resonance. This gas accumulation can then fuel star formation in a nuclear ring of "hot spots", which is a common observed phenomenon in barred galaxies. It is clear that gas inflows are more important in barred than in unbarred galaxies, since bars are often observed to be strongly impoverished of gas and star formation, both of which appear to have been moved towards the nuclear region of these galaxies (Larson 1994). Another possible mechanism for driving

at least sporadic inflows in galaxies involves dynamical friction, which can cause massive clumps of matter to lose energy and angular momentum and sink rapidly toward the center. A fourth mechanism that can drive rapid gas inflows in galaxies is the effect of tidal interactions, which can be especially effective because they can induce strong responses such as spiral patterns and bars in galactic disks that contribute to the outward transport of angular momentum and in add in they can produce a perturbation in the gravitational potential similar to that of a bar.
The fueling of nuclear starburst, which typically occurs a few hundred of the nucleus, may be explained on the basis of gravitational physics. It is also possible that similar mechanisms operate on much smaller scales and play a roll in the fueling of central BHs. Some simulations support this possibility [26, 40, 76]. Gaskell et al. [26] suggest that the accretion rate implied by the inflow is sufficient to power the AGN. The systematic change in polarization as a function of velocity across the Balmer lines suggests a net inflow of a scattering region somewhat exterior to the Balmer lines [26]. To get a net inflow of matter there must be outward transport of angular momentum. This means that something must apply a torque on the gas. This could be magnetic breaking caused by a wind [11] or a viscosity providing a torque between material at different radii. If we have inflow in the BLR, there is the same need for a torque to provide the necessary angular momentum transfer in the BLR gas. It would be natural for this to be provided by the same mechanisms as for the disk, i.e., magnetic breaking by a wind [26], or a magneto-rotational instability [4]. [26] suggest that the deduced mass inflow rates are comparable to the mass accretion rate needed to power AGNs and proposed that the BLR could be a major part of the material accreting onto the black hole.

1.6 Galaxy of study: UGC 2024

UGC 2024, earlier classified as an Sab galaxy [35] is more likely an SBab galaxy with a bar of ~ 8.95 kpc [47, 50]) and harbors a Seyfert 2 nucleus [75]. It is located at a luminosity distance of 90 Mpc [19], implying a linear scale of 0.436 kpc arcsec^{-1} (cosmology-corrected assuming $H_0 = 73 kms^{-1}Mpc^{-1}$, $\Omega_{matter} = 0.027$ and $\Omega_{vacuum} = 0.73$). A major axis position angle (hereafter PA) of 150° (from north to east) was derived by [65] via ellipse fitting to

Spectral Region	Absolute Mag or $\nu L \nu W$	Reference
Ultravilet	-16.95 $\pm$ 0.50 [mag]	Seibert, M. (2012)
Visual	-21.14 $\pm$0.50 [mag]	Sloan Digital Sky Survey Team
Near-Infrared	-23.55 $\pm$ 0.50 [mag]	Two Micron All Sky Survey Team
Mid-Infrared	9.78E+36 $\pm$ 1.97E+36 [W]	Moshir et al. (1990)
Far-Infrared	7.39E+36 $\pm$ 1.57E+36 [W]	Moshir et al. (1990)
Radio	9.51E+30 $\pm$ 2.07E+30 [W]	Condon, R. et al. (1998)

Table 1.1: Absolute magnitude data from NASA/IPAC EXTRAGALACTIC DATABASE

ground-based I-band images; their B-band images give a different major axis PA, but these images were shallower and more likely to trace [HII] regions rather than old stars. The inclination of the galaxy is 48°[1], computed from the apparent axial ratio listed in the UGC catalogue. The latest heliocentric radial velocity published for this galaxy is 6699 km/s^{-1}, i.e. a redshift z$\sim$0.022347$\pm$0.000010[2]. Older systemic velocity values vary between 6595 km s^{-1} [75] and 6728 km s^{-1} [25]. [28] determined the absolute linear diameter at the 25 B-mag arcsec^{-2} brightness level and the total blue luminosity, finding a diameter D$\approx$22.38 kpc and a luminosity of $L_B \approx 2.08 \times 10^{10} L_\odot$.

UGC 2024 presents emission line ratios of log([OIII]/Hβ) > 0.54, log([NII]/Hβ) > 0.46, and log(Hα/Hβ) > 0.55 [21], and is thus in the typical AGN region of the Baldwin-Phillips-Terlevich (BPT) diagrams [5]; log([NII]/Hα)> -0.3 [75].
Its photometric magnitud is 145 mag., on the other hand, the values for its visual, ultraviolet, near-infrared, etc. magnitudes are showed in table 1.1

Earlier studies of the optical continuum and the Hα emission-line by Heisler & Vader [32, 33] show that this galaxy presents a faint halo surrounding its nucleus. In the optical the galaxy shows two small spiral arms which extend into its faint outer halo [32], while in the Hα the spiral arms are not strong emitters. The latest leads to conclude that UGC 2024 is either an early type spiral or that

[1]https://ned.ipac.caltech.edu

[2]Sloan Digital Sky Survey Data Release 13 as obtained Jan. 31, 2017 from http://www.sdss.org/dr13/data_access/bulk/

the arms are tidal tails of older stars pulled out during a previous interaction [33]. On the other hand, unsharp masked and a B-R color images reveals many bright knots (H[II] regions) at either side of the nucleus along the same line as the spiral arms [32].

[64] found that UGC 2024 shows a diffuse [OIII] emission with no clear conical shape. The emission of this ionized gas is extended by $1.45\times$ 2.6 arcsec^2 (minor axis$\times$major axis extension) with the major axis along P.A.= -35°, within 5° from the host galaxy major axis. This galaxy presents only an unresolved and not extended nuclear radio source [38, 65] with a size < 45 pc [66] and also it shows weak broad lines in the NIR so it is not possible conclude if there exist dust-obscured broad lines [31]. [30] compared the spatial flux distribution of the [OIII] emission line with the Hδ absorption line spatial flux distribution to study the post-starburst region in UGC 2024. He stressed that, even if both fluxes have their peaks at the centre, Hδ is more extended at radius greater than $\pm$2". On the other hand, when he compared the equivalent widths (EWs) of these two lines, we can appreciate that the [OIII] EW ($\sim$6-12 Å) is larger than the Hδ EW ($\sim$3-5 Å) within $\pm$2", but then the Hδ EW stays almost constant whithin $\pm$4 arcsec. These two behaviors suggest that the post-starburst region in the galaxy may be more extended than the emission-line region. [30] also studied the Hβ EW, finding that this value is positive when the line is in absorption (at a distance > 1 kpc from the centre). Furthermore, he found that the [SII]/Hα flux ratio is peaked at the galaxy centre (in distances < 2", too). He finally concluded that these four features, flux distribution and EWs comparisons, Hβ EW and [SII]/Hα flux ratio distribution, suggest that the AGN and post-starburst regions are both centrally concentrated, but the post-starburst region is more extended towards the exterior of the galaxy than the emission-line region.

[27] found that the forbidden high-ionization lines ([FeVII], [FeX]λ6734Å, [FeXI]λ7892Å) as well as the lower ionization forbidden lines ([OIII]λ5007Å, [OI]$\lambda\lambda$6300,6363Å, [NII]$\lambda\lambda$6549,6583Åand [SII]$\lambda\lambda$6717,6731Å) in UGC 2024 are less redshifted than the host galaxy, that is, the velocities measured by fitting Gaussian models to each line are lower than the host galaxy recessional velocity, considering this as the [SII]λ6717,6731Åvelocity. They interpret the reduced recession velocities of the line-emitting regions as outflow velocities along our line of sight. However, they did not rule out the possibility of emission from infalling clouds approaching from the far side of the AGN.

[9] studied the dichotomy in the local radio AGN population with a sample of 18286 radio-loud active galactic nuclei. They investigated the difference between "High-excitation" radio galaxies and "Low-excitation" radio galaxies (HERGs and LERGs respectively) finding that exist a difference in the nature of the Eddington-scaled accretion rate on their central black holes: in HERGs is usual to find accretion rates between one per cent to 10 per cent of their Eddington rate, whereas in LERGs is usual find accretion rates below one per cent of their Eddington rate, which is consistent with models where the population separation is caused by a switch between radiatively efficient and radiatively inefficient accretion modes at low accretion rates. It is possible to appreciate that two population show differential cosmic evolution at fixed radio luminosity: HERGs evolve strongly at all luminosities and LERGs show weak or no evolution. They also analyzed the host galaxies of radio source finding support to the developing picture of radio-loud AGN: HERGs are fuelled at high rates through radiatively efficient standard accretion discs by cold gas, while LERGs are fuelled via radiatively inefficient flows at low accretion rates. However they do not show specific results for each galaxy, not even as an example or in a list, so it is complicated specify the classification they gave to UGC 2024.

[47] present a detailed visual morphology classification for galaxies in the Sloan Digital Sky Survey Data (SDSS) Data Release 4 (DR4, Cat. <II/267>). They found that UGC2024 presents a central bar with a length of 0.5 times the diameter of the galaxy and the inclination of the disk is between 50-70 degrees.

Chapter 2

Observations and data Processing

UGC 2024 was observed on December 01 2014 with the Integral Field Unit (IFU) of the Gemini Multi-Object Spectrograph (with the grating B600 of the Hamamatsu detector array) mounted on the GEMINI South Telescope (program ID: GS-2014B-Q-20, P.I. Neil Nagar). The observations consisted of one IFU fields covering 3.5 $\times$5 arcsec^2 around the nucleus with 0.08 arcsec sampling, centered on the nucleus and extended close along to the major axis position angle of the host galaxy (PA $\approx$ 150°. On the other hand, the observation was along an angle PA$_{obs}$ = 142°) so we think it is important for the understanding of coming figures that the "image major axis PA" is found at PA$_{img}$ = 8° counterclockwise direction from the y-axis. Four exposures of 900 s were obtained for each field, slightly shifted and dithered in order to correct for detector defects after combination of the frames. The seeing during the observation limited the spatial resolution to 0.5 arcsec, as measured from the FWHM of a spatial profile of the calibration standard, corresponding to 0.218 kpc at the galaxy distance.

The selected wavelength range was $\sim$4200–7300 Å, in order to cover the Hβ, [OIII]$\lambda\lambda$ 4959,5007Å, Hα, [NII]$\lambda\lambda$ 6548,6583Åand [SII]$\lambda\lambda$ 6717,6731Åemission lines, observed with the grating GMOS B600 (set to central wavelength of either λ 5700 Åor λ 5750 Å) at a spectral resolution of 75 km s^{-1}.

Data reduction was performed with IRAF[1] package provided by the GEMINI Observatory and specifically developed for the GMOS[2] instrument. The data reduction process included bias subtraction, overscan, flat-fielding, wavelength calibration (with errors of 2.4% and 1.5% for the arc centered in λ5700Åand λ5750Årespectively) and building of the data cubes at a sampling 0.08×0.08 arcsec^2/pixel. The final cube contains 2928 spectra with a final size of 3.84×4.88 arcsec^{-2} (48×61 spaxels^2).

Unfortunately, we got a gap in the centre of the [OIII]5007Åemission line in both images centered in 5700Åso, before combine the 4 cubes, we masked the spectra in a range of 64Åcentered in 5519Å, which is the central wavelength of the [OIII] line corrected by the redshift, in these two images. We did that to avoid the extrapolation of the line made by IRAF and therefore errors in the combination and the data analysis. However, the real intensity of the line is missed when combine the four cubes so we combined only those without the gap problem to do the analysis of [OIII]. Also, to do the analysis of the [SII] doublet was necessary to correct the lines of the effect of the B-band telluric lines. To do this we performed a black body curve using the V, R, I, J, H and K flux bands magnitudes of the standard star, then we divided the collided spectrum (a sum of all the spectra of the star in the data cube) by the synthetic curve to flat the star spectrum and finally we used this spectrum to divide every spectra in the galaxy data cube. By doing the last we were able to recover the flux in each [SII] line.

[1]IRAF is the Image Reduction and Analysis Facility, a general purpose software system for the reduction and analysis of astronomical data. IRAF is written and supported by the National Optical Astronomy Observatories (NOAO) in Tucson, Arizona.NOAO is operated by the Association of Universities for Research in Astronomy (AURA), Inc. under cooperative agreement with the National Science Foundation.

[2]http://www.gemini.edu/sciops/data-and-results/processing-software?q=node/11822

Chapter 3

Results

In the upper left panel of figure 3.1 we present the acquisition image of UGC 2024. The upper right panel is a zoom of the inner 3.84 $\times$ 4.88 arcsec^2, corresponding to the Field-of-View (FOV) covered by the IFU observation. In the middle left panel we present an structure map of an image obtained with the Wide Field Planetary Camera 2 (WFPC2) through the F547M filter aboard the Hubble Space Telescope (HST). The rectangle delimits the FOV. In the middle right panel we present a stellar continuum image from the IFU spectra obtained by integrating the flux in the lambda range 5235Å- 5710Åwhich correspond to the 90% passband of the F547M filter [1] of the HST. In the lower panels we show the spectra in each of the points in blue in the continuum image. This points represent the spectra of important zones, the ones with interesting features in kinematics (see figure 3.4), in Hα velocity map. Point 1 is the very nuclear point assumed as the peak of the continuum. Point 2 is an intermediate spectrum located in the redder region on the map. Both 1 and 2 were extracted from the cube resulting of the combination of the two cubes without the gap problem in the [OIII] stronger line. Points 3 and 4 are PA spectra and were extracted from the combination of all four cubes. Points 2, 3 and 4 were subtracted from regions in the velocity maps were the residuals are not null (see section 3.3).We can note that the [OIII] stronger emission line change its amplitude between the cubes, being smaller in the second one due to the lack of information of the line, information that we missed when we

[1]Data obtained from http://www.stsci.edu/hst/wfpc2/analysis/filters.html

masked the line .

All 4 spectra are typical of Seyfert 2 galaxies (more clear in the first and second spectra), showing [NII]λ6548,6583Å, [OIII]λ4363,4959,5007Å, [SII]λ6717,6731Å, [OI]λ6300,6363Å, Hα and [FeVII]λ6086Åemission lines. The spectrum from location 1 show narrow (average central velocity dispersion of $\approx$ 104 km s^{-1}) emission lines and a [NII]/Hα ratio of $\sim$0.96. The correction of the [SII] doublet is not showed in any of the spectra.

The structure map of UGC 2024 is an unsharp masked image of the F547M filter image obtained with the HST[2]. This shows the same two small spiral arms of which [32] talked about. This arms extend for approximately 6 arcsec each to the southeast and to the northwest. The same arms are visible in the acquisition image, where the arm to the SE is clearly thicker than the one to the NW. The green solid line show the PA of the galaxy following the NE square and the blue crux is marking the continuum peak. The continuum image (middle right) is smooth and symmetric respect to the position angle (black solid line).

3.1 Stellar Kinematics

To measure the stellar kinematics we used the Penalized Pixel-Fitting technique (**pPXF**, [12, 14]) with a subset of the MILES Library of Stellar Spectra [63], which contains 985 well-calibrated stars spectra covering a wavelength region from 3525-5700 Åat a spectral resolution of 2.51 Å(σ $\sim$64 km s^{-1}), to find the stellar continua which best fit to our data (that is, the best combination of templates for each spectrum). To do this ,and due to that the templates spectral resolution is different from the one of our data (σ $\sim$75 km s^{-1}), we debased the resolution of the templates to the GMOS resolution. Before the templates fitting, we binned the spatial axes of the cube using the Voronoi_2D_Binning[3][13] obtaining 822 bins with a minimum signal-to-noise ratio (S/N) of 25. In figure 3.1 we present an example of the fitted spectrum in the nuclear point of the galaxy (in red). To do more clear the visualization of the fit, we multiplied the stellar spectrum by 2 and by the same factor than the galaxy spectra (10^{15}) so the former is a little higher in the plot than the

[2]The image was downloaded from the Hubble Legacy Archive (http://hla.stsci.edu/hlaview.html).

[3]http:wwwastro.physics.ox.ac.uk/m̃xc/software/#binning

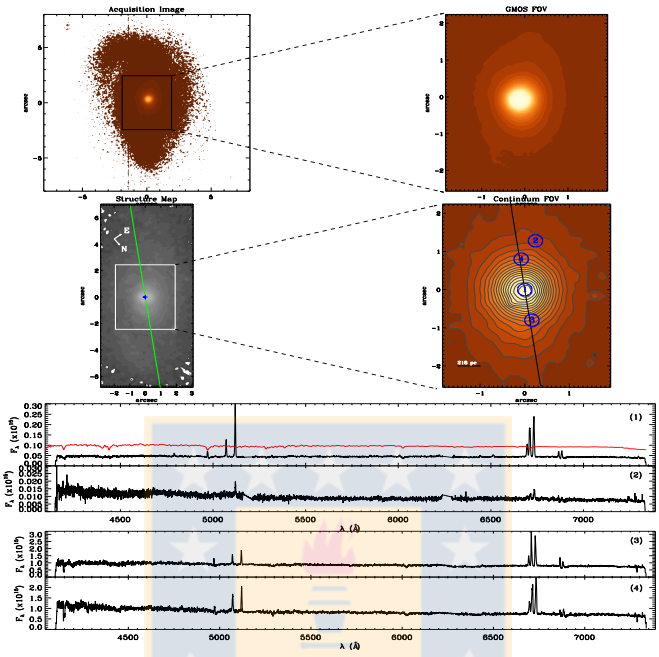

Figure 3.1: *Top left*: acquisition image.*Top right*: zoom of the acquisition image into the field of view of the GMOS-IFU observations. *Middle left*: structure map obtained from the HST image; the blue crux marks the nucleus and the green solid line shows the PA. The black and white rectangles delimit the FOV of the GMOS-IFU observations in the acquisition image and structure map respectively. *Middle right*: continuum image extracted from the IFU spectra; the solid black line indicates the position angle of the major axis (PA = 150°). The North-East squad is shown in the structure map and is the same in all images. *Bottom*: spectra of each of the marked points in the continuum image. The respective number is in the top left corner of each spectrum panel. Spectra 1 and 2 were extracted from the combined cube with only the cubes without the [OIII] problem with the gap. Spectra 3 and 4 were extracted from the combined cube with all four initial cubes (with a masked [OIII]). From this work.

second.

The stellar rotation is shown in the left panel of figure 3.2 with velocities ranging from ∼-124 to 117 km s^{-1} assuming a systemic velocity (v_{sys}) of 6780 km s^{-1}. The maps does not show the complete FOV since the pixels in the edger 0.5 arcsec have a very low S/N so the pPXF routine could not fit

fine the stellar continuum on those. The centre is marked with the intersection of the solid and dashed black lines and is assumed as the peak of the continuum. We modeled the stellar kinematics assuming circular orbits in a plane and spherical potential [8]. The observed radial velocity at a position R, ϕ is given by:

$$VR, \phi = V_{sys} + \frac{AR\cos\phi - \phi_0}{R^2\sin^2\phi - \phi_0 + \cos^2\theta\cos^2\phi - \phi_0 + c^2\cos^2\theta^{p2}}$$

where θ, ϕ, V_{sys} and R are known values (inclination of the disk considering $\theta = 0$ for a face-on galaxy, the PA of the line of nodes measured from the y-axis within the FOV, the systemic velocity and the radius, respectively) and A, c and p are parameters of the model. Table 3.1 show the fitted values of all the parameters. ΔV_{sys} is the velocity found in zero radius, assuming the central point as the peak of the continuum. To fit the rotation velocity, it means, to fit the parameters to the velocity field we used the Levenberg-Marquardt least-squares algorithm. The final model and residual velocity field (fitted pPXF velocity - model$_*$) are in the second and third panels of figure 3.2 respectively. The residual shows that the stellar kinematics is dominated by pure rotation, with no special features. The velocity dispersion map is the fourth panel in the same figure and has values from 0 in the outer 1.2 arcsec to the S and SE increasing to 180 km s^{-1} in the nuclear part.

With the mean stellar velocity dispersion within a circumference of 0.115 arcsec (50.14 pc) radius, centered on the nucleus, we got an estimation of the mass of the central black hole. We used the M-σ relation [44]

$$M_\bullet M_\odot = 1.3\left(\frac{\sigma_\star}{200\ km\ s^{-1}}\right)^{4.72} \times 10^8$$

with $\bar{\sigma}$ =173 km s^{-1}. This velocity dispersion leads us to a mass of the SMBH $M_\bullet = 6.55 \times 10^7$ $M_\odot$.

This value must be considered as an approximation of the mass since the influence radius of the BH is significantly lower than 50 pc ($r_h \equiv GM\sigma^2 \rightarrow$ $r_h \sim 11$ pc for $M_\bullet = 10^8$ $M_\odot$ and $\sigma = 200$ km s^{-1}).

Table 3.1: Bertola Parameters - Stellar and Gas Components

Parameter	Fixed ($\star$)	Fitted Value ($\star$)	Fixed (Hα)	Fitted Value (Hα)
ΔV_{sys}	no	45.16 km s^{-1}	yes	10 km s^{-1}
ϕ_0	yes	8°	yes	8°
θ	yes	48°	yes	48°
A	no	170 km s^{-1}	yes	500 km s^{-1}
c	no	0.841	yes	1
p	no	0.935	yes	1.9

Notes.-Values for the parameters of the star rotation model. Column 1: Parameter name. Column 2: If the parameter has a fixed value or not for stellar rotation. Column 3: Final fitted Value for stellar sotation. Column 4: If the parameter has a fixed value or not for gas rotation. Column 5: Final fitted value for gas rotation.

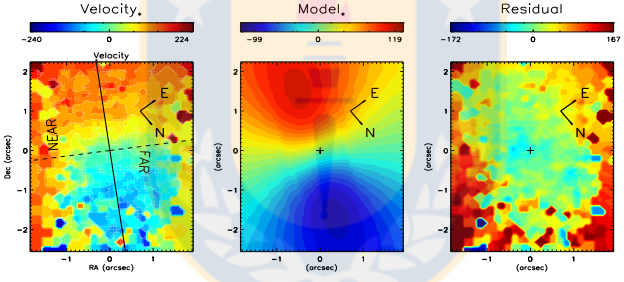

Figure 3.2: From left to right: stellar velocity (km s^{-1}) obtained with pPXF. Binning was applied to get a minimal S/N of 25, Bertola model for stellar rotation, residual (velocity - model) and stellar dispersion velocity (km s^{-1}). The solid (dashed) black line indicates the major (minor) axis. The intersection between minor and major axes is in the peak of the continuum. The panels follow the color bar on top. From this work.

3.2 Single Gaussian Emission Line Fitting

We used IDL[4] routines to model emission lines and the stellar continuum (see section 3.1). We derived the centroid velocities, fluxes and velocity dispersions of the stronger emission lines (Hβ, [OIII]λ5007Å, Hα, [NII]$\lambda\lambda$6548,6583Åand [SII]$\lambda\lambda$6717,6731Å) by using PROFIT. This routine fits single Gaussian profiles to each line. We used air rest frame wavelengths and we corrected them by redshift (z$\sim$0.0226) to use as initial guess. Seven separate runs were performed to fit Hβ, [OIII], [OI], Hα, [NII]λ6583Åand the [SII] doublet.

Figure 3.3 presents the rotation curves for the important emission lines and for the stars. These curves were constructed by extracting the velocities within the FOV through the host galaxy PA after the subtraction of a velocity of 6780 km s^{-1}. The curves show that every emission line is blueshifted respect to the host galaxy, with differences in velocities of $\sim$-83 (Hα) up to $\sim$-8 ([OIII]λ4958Å) km s^{-1} in zero radius, using as reference the velocity at the continuum peak. In a general view, velocities are located between $\sim$-150 km s^{-1} and $\sim$170 km s^{-1}. In section 3.3 we will see that the amplitudes of the velocities in Hα and [NII] are larger, but there is a zero component velocity which is pulling down (and up) the extremes of the curves.

Inspecting the rotation curves and the velocity maps we noted asymmetries in all emission line velocities showing almost pure flat rotation curve in negative radii (north) and curves similar to solid body rotation going back to flat in positive radii (south). Anyway, the emission line rotation curves get all together at $\sim$0.3 arcsec from the nucleus through the major axis PA.

Figure 3.4 presents the integrated flux (erg s^{-1} cm $^{-2}$ spaxel $^{-1}$), velocity field and velocity dispersion of [OIII], Hα and [NII] emission lines obtained by fitting single Gaussians to the lines. The zero velocity in centroid velocity maps correspond to a systemic velocity of V_{sys} = 6780 km s^{-1}. We fixed the major axis PA as 150° in agreement with [65] because this value represents the best our data.

Fluxes are in the first column of figure 3.4. While [OIII] presents the peak of the emission in the nucleus, Hα and [NII] have their peaks at $\approx$0.25 arc-

[4]Interactive Data Language (IDL) is a programming language used for data analysis and visualization.

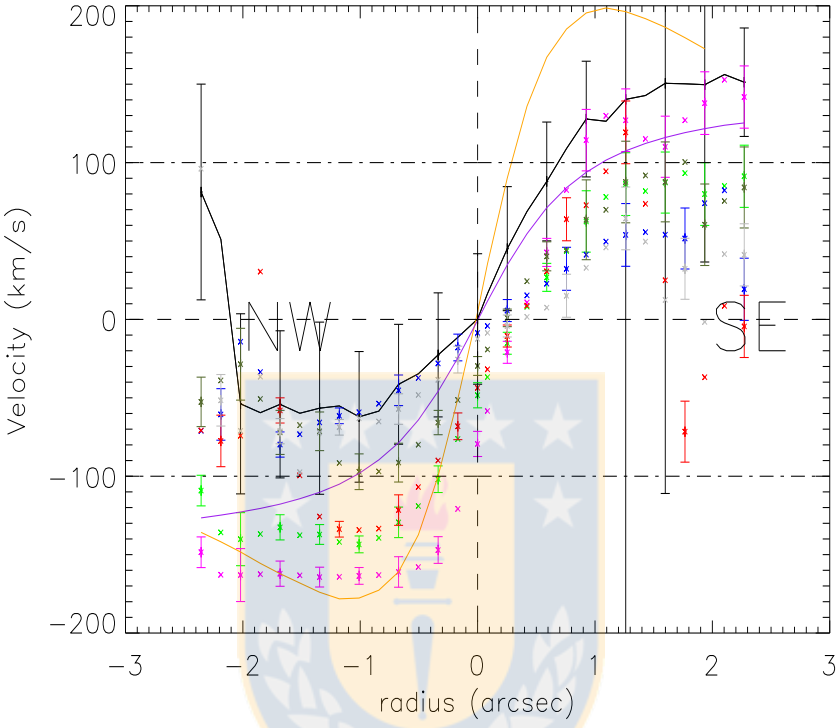

Figure 3.3: Rotation curves for SII (dark green), NII (green), OIII (blue), Hα (magenta), Hβ (red), stellar component black solid line). Velocities where extracted throughout the host galaxy major axis PA = 150° counterclockwise assuming the centre of rotation as the point were the continuum peak is located. The stellar error bars show the errors determined by pPXF. From this work.

sec going down through the major axis PA. Also, they have little differences in structure. Hα (top) flux is clearly asymmetric and extended to the NE, [NII] (middle) flux seems to be symmetrical respect to the major axis and, as reported by [64], [OIII] (bottom) flux is kind of symmetric respect to the emission line PA but more extended through the major axis. The flux extensions in the major and minor axes for each line are 3.0×3.1 arcsec^2 (Hα), 3.2×3.7 arcsec^2 ([NII]) and 3.1×3.5 arcsec^2 ([OIII]). The extension in [OIII]

is significantly larger than the one found by [64] which can be attributed to the the way the data was obtained, since HST used a filter to take the images we have the complete spectrum for each of the spaxel covering the nuclear region, so we do not lose many information.

Centroid-velocity maps are in the second column of figure 3.4 and they all show velocity fields dominated by rotation. The black crux marks the peak of the continuum. Hα and [NII] present similar shapes but the former has and excess of redshift in the SE and of blueshift in the NW respect to the second. This two lines have velocities that go from $\approx$-180 up to $\approx$180 km s^{-1}. On the other hand, [OIII] shows an homogeneous velocity field and the lower velocities of the three lines between $\approx$-100 and $\approx$100 km s^{-1}. We also noticed that no line have zero velocity in the nuclear region, being all the central velocities less redshifted than the host galaxy (seen more clearly in figure 3.3). [27] referred to this and point out that it could be possibly due to outflow velocities.

The intrinsic velocity dispersion was derived as

$$\sigma_{int} = \sqrt{\sigma_{obs}^2 - \sigma_{ins}^2}$$

where σ_{obs} is the observed velocity dispersion derived by the emission line fitting and σ_{ins} is the instrumental velocity dispersion. [OIII] presents a smooth velocity dispersion map. On the other hand, Hα and [NII] have a non common distribution of their velocity dispersions. In Hα the values are higher around the bluer and the redder velocities. [NII] presents two peaks, one at 0.3 arcsec to the N of the continuum peak and the other at 1.1 arcsec to the SE from the same point.

3.3 Position-Velocity Diagrams

We built Position-Velocity (PV) diagrams to better understand what is going on in the centre of UGC 2024. Figure 3.5 shows the diagrams extracted from Hα+[NII]λ6583Åand [OIII] through the major and minor axes and several other angles named on the figure. The angles are measured from the y-axis in counterclockwise direction. Hα presents a bump in blue velocities in every angle but in a deeper study of this strange feature we discovered that it is caused by an error in the CCD (working to fix it ERASE). We compared PV

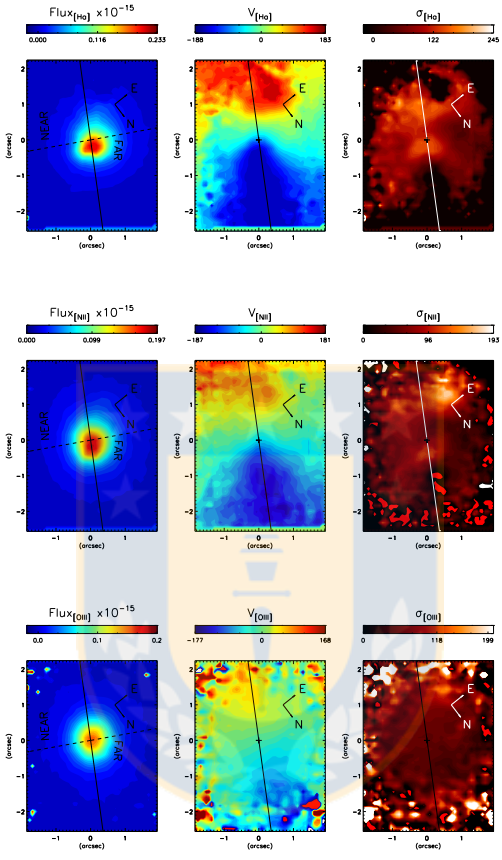

Figure 3.4: From left to right: maps of the flux (units of 10^{-15}erg s^{-1} cm^{-2} spaxel^{-1} following the color bar at the top of each panel), velocity (km s^{-1}) and velocity dispersion (km s^{-1}) derived from the single Gaussian fit to the Hα (*top row*), [NII]$\lambda\lambda$6583Å(*middle row*) and [OIII]λ5007Å(*bottom row*). Axes (in arcsec) are relative to the stellar continuum peak, indicated by the intersection of the solid and dashed lines in the flux maps and the black cross in the velocity and velocity dispersion maps. The solid (dashed) line indicates the major (minor) axis. The near (SW) and far (NE) sides of the disk are marked in the flux maps. Each panel follows the color bar on top. The zero velocity corresponds to a recessional velocity of 6780 km s^{-1} . From this work.

diagrams of this line in every single cube before combine them and found that the feature is present only in two of the four primary cubes, and this cubes share the spatial position centering on the observation configuration but they do not share spectral centering so we ignore the bump in the interpretation of the results. We did not discard the final Hα emission line obtained by combine the four cubes because if we had done that the S/N would be not high enough. (probably have to change this part when find the way to mask the bad channels)

We over plotted the emission line rotation curves (white line) and realize that the velocities found by fitting a single Gaussian are not representative of the real behave of the line. If we ignore purple and red lines it is appreciable that the velocities obtained by a single Gaussian only fit negative velocities amplitude but do not get the higher ones revealed by the PV diagram. We think that a second component with lower velocities than the ones of rotation is "confusing" the single Gaussian fit pulling down the "red values".

We produce a lot of "fake" Bertola models (because the parameters were not adjusted to better represent the Hα single Gaussian velocity field) to find one which better fit the rotation, that means, the velocities we observed on the Hα diagrams. We focused on fit the major axis PV diagram reveled rotation curve, with its high amplitude and the values for the parameter of the best fit are shown on table 3.1. The rotation curves extracted from the final Bertola velocity field were overploted in its corresponding diagram. We only care about the major axis but while the angles start to change the modeled rotation curve changes as well and it adjust quiet well to the diagrams. We also overploted the stellar Bertola model rotation curves in every angle-PV diagram to realize if in some point the gas motion is dominated by stars, but it stays clear that this is not happening in any of the directions showed.

The second column of figures 3.6 and 3.7 show the gas bestfit fake rotation model we performed by forcing the parameters to fit the velocity showed by the Hα PV diagram and the third column shows the residual (observed-fake model) velocity fields for Hα and [NII] with [OIII] (first and second row) in each respectively figure. In both figures we show the velocity map obtained by fitting a single Gaussian to Hα, [NII] and [OIII]. Hα presents an excess of redshift to the SE and other with lower velocities to the NE with velocities of nearly 80 km s^{-1} and 26 km s^{-1} respectively and an excess of blueshift to

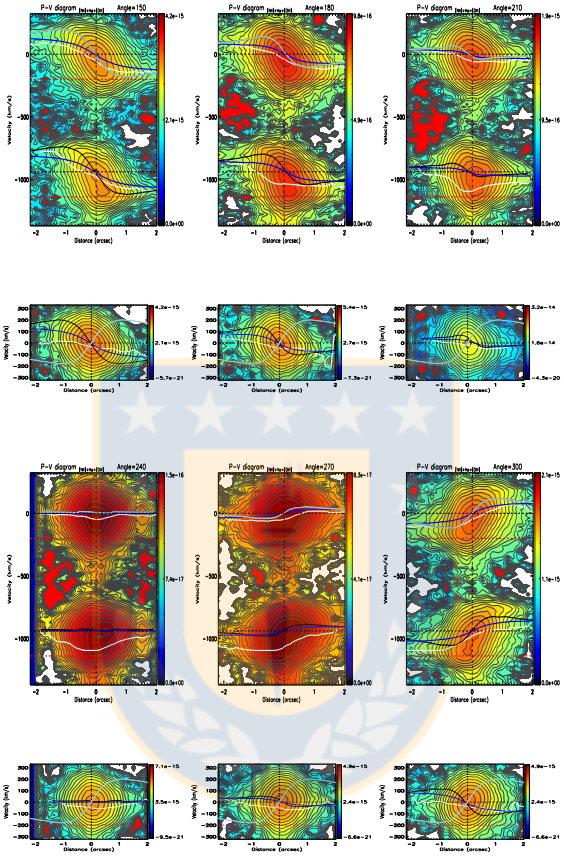

Figure 3.5:]

PV diagrams of the Hα +[NII] (continuous pv diagram: [NII] at the top + Hα at the bottom) and [OIII] emission lines. The angle in each panel title is the PA on the sky. The *x*-axis is the offset, in arcsec, from the stellar continuum peak, with the nuclear position delineated by the vertical dashed black line. The *y*-axis, in units of km s^{-1}, is relative to the adopted recessional velocity (6780 km s^{-1}) ; the zero velocity is delineated by the horizontal dashed black line. In the Hα +[NII] diagram the zero velocity is set to that of the [NII] line; the zero velocity for the Hα line, calculated as an offset from the [NII] line assuming the same recessional velocity, is also marked with a dashed black line. Horizontal dashed red lines are drawn at -200 km s^1 only as a guide to the eye. On each diagram we overplot the velocity predicted by the single Gaussian fit (white solid line), the prediction of the Bertola rotation model for the stars (blue solid line) and the best (by eye) Bertola rotation model for the gas (black solid line). From this work.

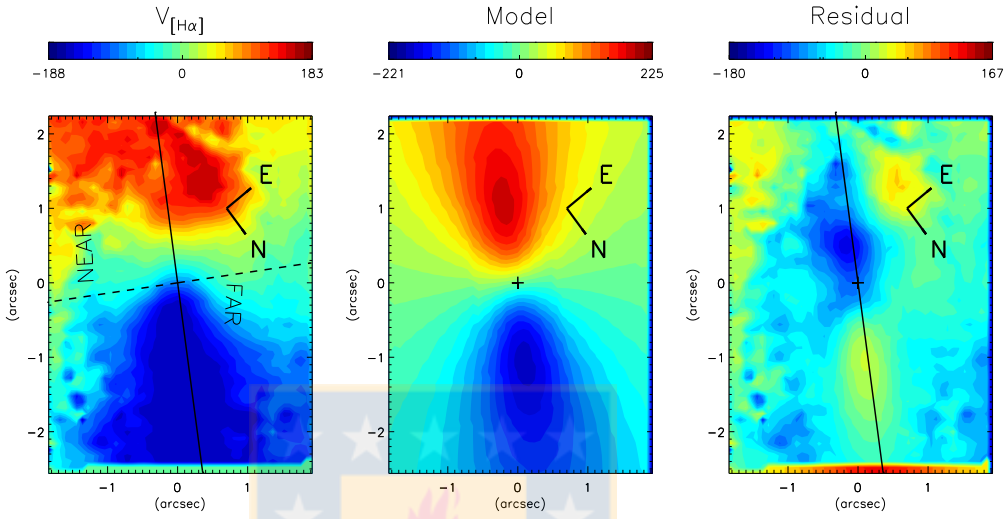

Figure 3.6: From left to right: Observed Hα velocity map, fake Bertola model and the residual velocity map (observed - fake model). Each panel follows the colorbar on top in km s^{-1}. In the first panel the black solid and dashed lines show the host galaxy major and minor axes of the host galaxy whit the intersection in the continuum peak. The solid line in the residual map indicates the major axis. The model was forced to follow the rotation observed in Hα PV diagrams. From this work.

the SW with velocities that reach $\sim$-140 km s^{-1}. [NII] and [OIII] present also deviations from pure rotation. In the case of [NII] the residuals are aligned with the host galaxy major axis and they reach velocities of $\sim$44 km s^{-1} to the NE and $\sim$-149 km s^{-1} to the SW. Finally, [OIII] present perturbations through the major axis PA too, but at the external radius these seem to tilt, leaving the alignment with the major axis. The more extreme values of the [OIII] residual are $\sim$125 km s^{-1} to the SW and $\sim$-150 km s^{-1} to the NE.

3.4 Gas Excitation and Electron Density

We compute emission line ratios dividing flux maps obtained by fitting a single Gaussian. Figure 3.8 shows [OIII]/Hβ and Hα/Hβ in log scale, [NII]/Hα,

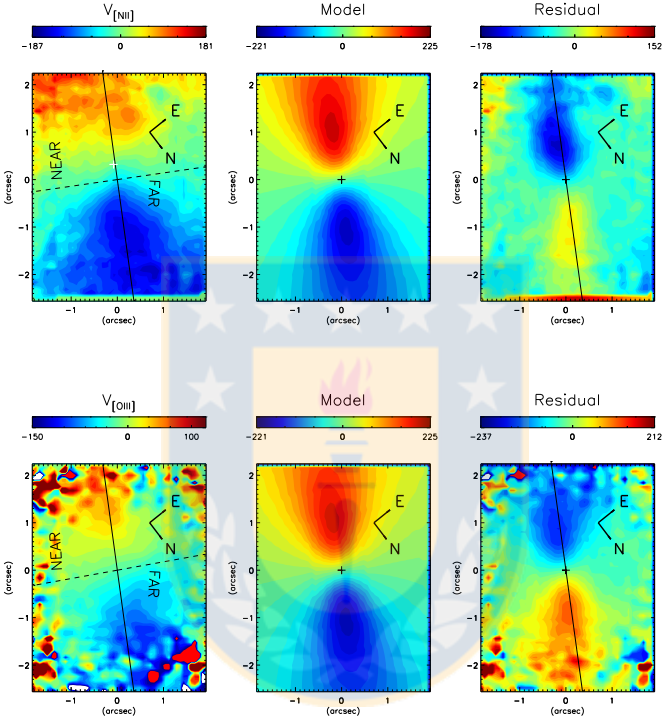

Figure 3.7: ,
bottom: [OIII])...]From left to right: Observed velocity map (top: [NII], bottom: [OIII]) obtained by fitting a single Gaussian, fake rotation model and the residual velocity map (observed- fake). Each panel follows the colorbar on top in km s^{-1}. In the first panel the black solid and dashed lines show the major and minor axes of the host galaxy whit the intersection in the continuum peak. The solid line in the residual map indicates the major axis. From this work.

OI/Hα and the electron density as derived from the intensity ratio[SII]λ6717/λ6731 assuming a temperature of 10^4 K [49]. We selected only the inner 1" radius as this is the average radius where all the emission lines present better S/N (>10).

Since we did not have previous information about the way in which the galaxy is inclined we used this ratios to decide if the near side was either to the NE or to SW. It is clear that all ratios present higher values to the SW, but we are interested specially in Hα/Hβ ratio to determine where the near and far sides are. The values of this ratio increases westwards going from $\sim$2.5 up to $\sim$8 which implies that the far side could be to the NE and the near to the SW. This has been our convention in the whole paper. The [NII]/Hα ratio ranges from $\sim$0.77 ($\log_{10}$: -0.113) to $\sim$1.39 ($\log_{10}$ 0.143) within the inner 1" radius with a value of $\sim$0.966 in the nucleus ($\log_{10}$: -0.015). [OIII]/Hβ behaves in a similar way, decreasing from SW to NE with values between $\sim$3.54 and 13.49 (in $\log_{10}$ 0.5 and 1.13) in the inner 1" radius and a value of $\sim$7.43 ($\log_{10}$: 0.87) in the nucleus. This ratio values are typical of Seyfert galaxies [37] if we locate then in a BPT diagnostic diagram.

The electron density map presents not clear circular distribution reaching its peak at 0.3 arcsec eastwards from the nucleus with a value of 1511 cm^{-3} decreasing to 726 cm^{-3} at the nucleus and going lower with radius northwards presenting values of 200 cm^{-3} at 1" radius(considering zero radius in the electron density peak). The extremely high values to the SW are due to high noise, which impedes a reliable and good single Gaussian fit, anyway we did not limit the radius to other smaller than 1" because we would be loosing even more the general view of the electron density behave.

3.5 Double Gaussian Fit

Since the PV diagrams evidence a second velocity component in Hα and [NII] we performed a double Gaussian fit to this lines. figure 3.5 shows clearly that the second component is always blueshifted from the pure rotating one we force the second component to be bluer than the main one. We performed double Gaussian fits to Hα isolated and to Hα+[NII].

Results of the fitting are shown in figure 3.9. For Hα we selected the isolated fit. On the other hand, the bound fit was better enough for the stronger [NII] line so it was not necessary to do an isolated fit of this line. Fluxes of

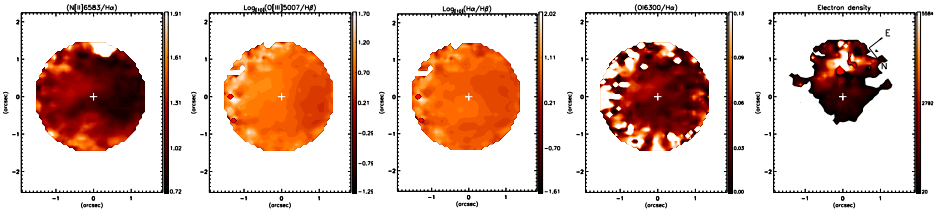

Figure 3.8: /
Hα, [OIII]/Hβ, Hα/Hβ, [OI]/Hα line ratios and electron density (cm $^{-3}$) distribution...][NII]/Hα, [OIII]/Hβ, Hα/Hβ, [OI]/Hα line ratios and electron density (cm $^{-3}$) distribution. [OIII]/Hβ and Hα/Hβ are in logarithmic scale. The white crux in each image point the centre peak of the continuum. The panels follow the color bar to the right of each one. All panels follow the orientation of the N-E squad in the electron density image. From this work

the second components in both lines present kind of circular distribution with their peaks near the centre. Hα main component has its peak at the centre (black crux) but it is extended to the near side. [NII] main component has a peak to N and a second weaker peak in the very centre.

Velocities of the main components show pure rotation aligned with the major axis PA, while the Hα second component presents rotation, but only in negative velocities respect to the main recessional velocity. Also its orientation is deviated from the major axis PA. [NII] second component velocity is aligned with the major axis and presents rotation but, as Hα, only has negative velocities.

We plotted the rotation curves extracted through the major axis in the PV diagrams of the major axis of Hα and [NII] (figure 3.10). Rotation curves of the single Gaussian and main component are very similar in both cases and neither of the curves reach the highest values in the diagrams. The second components present a different behave. $H\alpha_{second}$ velocities in the inner 0.9 arcsec (distance from nucleus) are redder than the velocities of $H\alpha_{main}$ ones, but the velocity amplitude is lower, so it does not reach the maximum and minimum values of the rotation. On the other hand, $[NII]_{second}$ presents always bluer values respect to the $[NII]_{main}$ velocities.

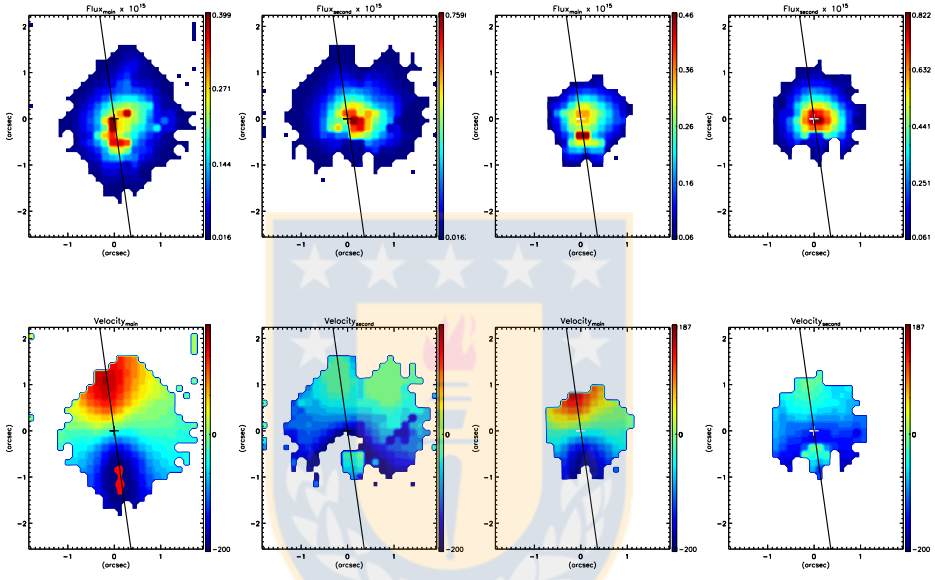

Figure 3.9: On top figure shows fluxes and in bottom it shows velocities corresponding to the main and second Gaussian component of Hα (first and second columns) and to the main and second component of [NII] (third and fourth columns). We masked Hα plots in a flux of 1.7×10^{-17}erg s^{-1} cm^{-2} spaxel^{-1} and NII in a flux of 6×10^{-17}erg s^{-1} cm^{-2} spaxel^{-1}. Fluxes are in units of 10^{-15}erg s^{-1} cm^{-2} spaxel^{-1} and velocities are in km/s. Every pannel follows the colorbar to its right. Solid black line marks the major axis PA, while the black crux is pointing the centre (assumed as the peak of the continuum). From this work.

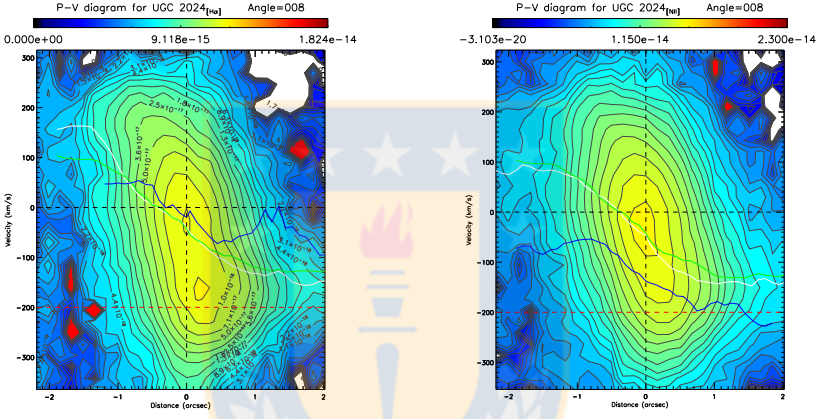

Figure 3.10: P

V diagram of the major axis...]Left: HαPV diagram of the major axis. Right: [NII] PV diagram of the major axis. White solid line is the rotation curve of the single Gaussian fit. Green solid line is the rotation curve of the main component in the double Gaussian fit and blue solid line is the rotation curve of the second (blue) component in the double Gaussian fit. Black and red dashed lines follow the convention of figure 3.5. From this work.

Chapter 4

Discussion and Summary

The continuum image in figure 3.1 as well as the zoom of the acquisition image show that the light distribution of the galaxy is more extended to the SW than to the NE in the inner 1.5 arcsec radius, changing to a more homogeneous distribution at larger radius. The acquisition image show a big and thick arm to the S which vanished at $\sim$5" and other to the N with approximately the same extension. The latest one is not so clear but it looks like a bump in the image. The two arms are more clear in the structure map, where we can clearly see the second arm ricing in the W and extending itself to the N. Also we can observe that both arms reach $\sim$6" until they faint. The arms become less distinguishably towards the nucleus and they are not visible in the GMOS-IFU FOV continuum. Due to the post-starburst nature of the galaxy [30] and that this past starburst phase could be triggered by a previous interaction, we think that this arms can effectively be tidal tales of older stars pulled out during that merging process [33]. Also, as the arm to the S is thicker and stronger than the one to the N we propose that that (*probably minor*) merger occurred in the S of UGC 2024. If we compare the position of the arms with all the velocity maps we can observe that one is placed in blue velocities and other in red ones. Both, velocity position and shape of the arms are signatures of trailing arms [10]. Now, if we talk about the inner structure we can hardly appreciate the dust towards the SW but these is highlighted by the irregular contours present in the structure map and confirmed by the extension of the light distribution in the continuum and in the acquisition image. This confirm what we argue in section 3.4, were we defined the near and far sides using the emission line

ratios. Likewise, the structure presents a little arm at $\sim$1.5 arcsec eastwards, this tiny arm change its orientation outer that radius and pass to be part of the thick arm southwards, so we can mostly assure that the southern arm is born in the E part of the galaxy.

[64] argue that the [OIII] distribution presents a not clear conical shape, but a biconical shape is what we expect to find in the ionized line distribution of Seyfert 2 galaxies [2]. Anyway, from the PV diagrams in section 3.3 we found a second component in this line as well as in Hα and [NII] with lower velocities than the ones observed by pure rotation in red velocities (negative radii on the PV diagrams) showing that the single Gaussian fit velocities are being biased by this component since the rotation curves do not reach the highest velocity of the PV diagrams. This can be a tracer of an outflow with low velocity but high velocity dispersion. Even if [OIII] presents a well behave in the PV diagram it also shows a tilt, changing its orientation in larger velocities (blue and red ones).

[78] studied the extended narrow line region (ENLR) in 7 Seyfert galaxies, this region is located typically at distances > 500 pc. These galaxies are characterized by a high excitation ([OIII]/Hβ $\geq$5) but low velocities dispersion. If the tendency to increase outwards of the [OIII]/Hβ ratio is the general behave in the galaxy, we can argue that UGC 2024 has an excitation > 6 out 1" radius (> 436 pc). Furthermore, evidence of radial outflow has been reported in galaxies that presents this ENLR characteristics [85]. The [OIII] velocity profile coincide with some of the objects in [78], with velocities of $\sim$200 km s^{-1}. Also, the residuals of figures 3.6 and 3.7 added to the PV diagrams reveal outflowing gas with higher velocities at the major axis and decreasing outwards. With all the last we can propose that UGC 2024 presents a radial outflow.

4.1 GMOS and SDSS Velocity Shift

We collided the spectra within 1.5 arcsec of the GMOS cube before the subtraction of the continuum and compared the resulting spectrum with the SDSS one[1] which was taken in October, 2000. We computed velocities for Hβ, [OIII]$\lambda\lambda$4958,5007Å, [OI]λ6300Å, Hα, [NII]$\lambda\lambda$6549,6583Å, [SII]λ6731Åemission lines and for the NaID absorption line. We find the center of the lines by fitting

[1]We used the Sloan Digital Sky Survey Data Release 7 spectrum of UGC 2024.

a single Gaussian to each one in the IRAFTERM plot of the spectra (using the IRAFTERM tasks). The velocities of each line in the SDSS data were obtained using vacuum rest-frame wavelengths while the velocities of the GMOS data were obtained using air rest-frame wavelengths. In figure 4.1 we show the obtained velocities (x-axis), the cruxes(diamonds) represent SDSS(GMOS) results and they are arranged in the y-axis from minor (bottom) to major (top) wavelength. To have an homogeneous way to contrast the results we chose the [SII] velocity (V_{SII}) as the recessional velocity of the galaxy in both cases, since it is less affected by ionization. It is clear that exist a difference between SDSS and GMOS (the velocity shift is $\sim$58 km s^{-1}). As reported by SDSS, forbidden lines present less blueshifted velocities (using as reference the V_{SII}) than Balmer lines in both spectra and the pattern followed by the velocities is similar so we discarded calibration errors that can end in such a big velocity difference between the data.

If we consider V_{SII} obtained with the GMOS data, the redshift would be z_{new} $\sim$0.0226, value that is far from the ones found in literature [9, 25, 35, 42, 75] and specifically, it differs from the SDSS DR13 value, z_{SDSS}=0.022347$\pm$0.00001, by an amount of $\sim$81 km s^{-1}. It is important to note that the recessional velocity computed from the SDSS [SII] line was also shifted from the value of the 13th data release, being $\sim$23 km s^{-1} higher.

In figure 4.1 is also evident a big blueshift ($\sim$188 km s^{-1}) respect to V_{SII} in the star velocity (NaID) in both SDSS and GMOS. We will discuss about this shift in section 3.1.

4.1.1 Mass Outflow Rate

We estimate the mass outflow rate as the ratio between the mass of the outflowing gas and the dynamical time at the nucleus ($M_g t_d$). The gas mass is estimated as:

$$M_g = m_p N_e V f \tag{4.1}$$

where m_p is the **proton mass**, N_e is the **electron density**, V is the **volume of the region where the outflow is detected** and f is the **filling factor**. We can estimate the filling factor from:

$$L_{H\alpha} \sim N_e^2 j_{H\alpha} T V f \tag{4.2}$$

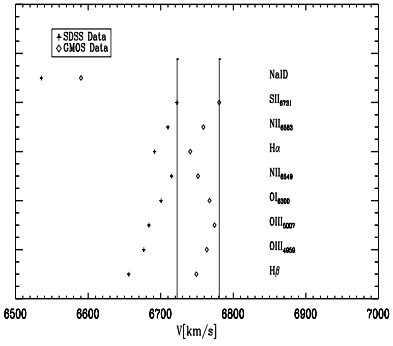

Figure 4.1: Comparison between the velocities of the most important emission lines + NaID absorption line computed with the SDSS DR7 spectrum (cruxes) and a 3" aperture of our GMOS data spectrum (diamonds). With SDSS data we used vacuum rest-frame wavelengths and with GMOS data we used air rest-frame wavelengths to compute the velocities. The black solid line at 6707 km s^{-1} correspond to the velocity of the [SII]λ6731Åemission line of SDSS and the one at 6780 km s^{-1} marks the velocity of the [SII]λ6731Åemission line of GMOS. The labels to the right indicate the emission(absorption) lines names. From this work

with $j_{H\alpha} = 3.534 \times 10^{-25}$ erg cm^{-3} s^{-1} at T=10000 [48] and $L_{H\alpha}$ the Hα luminosity emitted within the volume V. Then if we substitute equation 4.2 into equation 4.1, the mass can be expressed as:

$$M_g = \frac{m_p L_{H\alpha}}{N_e j_{H\alpha} T} \tag{4.3}$$

The second velocity component is the broader one and is which represents the better the outflow [41], so we used the Hα_{second} mean velocity to obtain the luminosity of the line. The mean deprojected velocity of the second component of Hα is 123 km s^{-1} and from the residual in figure 3.6 we decided that the radius where the outflow is influencing the gas rotation is $\sim$1". Considering a luminosity distance of 90 Mpc, $L_{H\alpha}$ value is 1.709×10^{41} erg s^{-1}. We use the mean N_e within a 1" radius, that means, N_e = 1312 cm^{-3}. Then we computed a ionized gas mas of $M_g \approx 3.26 \times 10^5$ $M_\odot$ for the outflow component. Now, taking into account that we are only measuring the mass of one cone and general models predict bi-conical outflows, then the mass associated

to the ionized gas should be 6.53×10^5 $M_\odot$, which is the amount of gas responsible of the second (broad) Hα emission.

We estimate the dynamical time as the ratio of the diameter of the region where the outflow is observed (1" $\approx$ 436 pc) to the mean deprojected velocity of the outflow (123 km s^{-1}). This gives a $T_d \approx 7.1\times10^6$ yr so the mass outflow rate M is 0.046$M_\odot$ yr^{-1}. For comparison, the mass accretion rate implied by the bolometric luminosity, M_{acc}, can be estimated by:

$$M_{acc} = \frac{L_{bol}}{\eta c} \tag{4.4}$$

where L_{bol} was obtained using [23] relation between [OIII] luminosity and bolometric one: $L_{bol} = 90\times L_{OIII}$ what implies a $L_{bol} \approx 9.02\times10^{42}$ erg s^{-1}, with $L_{OIII}=1\times10^{41}$ erg s^{-1}, η is the mass-to-energy conversion efficiency, assumed as 0.1 [70] and c is the speed of light in cm s^{-1}. Replacing all this values in equation 4.4 lead to a mass accretion rate of $M_acc \approx 1.59\times10^{-3}$ $M_\odot$ yr^{-1}. This mass is only 0.034 times the mass outflow rate, which is within the values found in previous studies [41, 57, 68] and indicates that the most of the outflowing gas originate in the surrounding interstellar medium.

4.2 Summary

In this section we are going to enumerate the main conclusions of the thesis:

- Considering the gas excitation, structure map and continuum profile we conclude that the near side located towards the SW and the far to the NE.
- UGC 2024 does not present correlation between Hα and [OIII] kinematics. It is usual to see features of the former line in the other, but we think this is due to the lack of information because of the gaps present in two of the four original cubes.
- Residuals of Hα and [NII] indicate that the gases are not following normal (pure) rotation, having the higher disruptions through the major axis.

- In comparing the Bertola rotation models of the gas and stars, this two rotational components are not moving at the same velocity, which means the second has perturbation that can be explained by outflowing gas.

- PV diagrams reveal a second component in Hα, [NII] and [OIII]. With a double Gaussian fit we were able to isolate both (in Hα and [NII]) and study individually their behavior. The second components have bluer values in velocity but higher velocity dispersion, so we propose a wide open angle outflow to rep

- Hα and [NII] single Gaussian velocity maps present clear perturbation of a bar, but the S/N of the galaxy was not high enough to get a good model of the bar and its possible effect over the centre of the object.

- The outflow present on UGC 2024 is weak in comparison with the ones reported in the literature and, even if this value is within the range where Dumas et al. 2007 [23] found more disturbed kinematics, the galaxy does not presents big misalignments between the gas and the stellar kinematics nor large twists in the gas kinematics.

Bibliography

[1] R. ANTONUCCI, *Unified models for active galactic nuclei and quasars*, araa, 31 (1993), pp. 473–521.

[2] H.-J. BAE AND J.-H. WOO, *The Prevalence of Gas Outflows in Type 2 AGNs. II. 3D Biconical Outflow Models*, apj, 828 (2016), p. 97.

[3] J. N. BAHCALL, M. SCHMIDT, AND J. E. GUNN, *Are Some Quasi-Stellar Objects Associated with Clusters of Galaxies?*, apjl, 157 (1969), p. L77.

[4] S. A. BALBUS AND J. F. HAWLEY, *A powerful local shear instability in weakly magnetized disks. I - Linear analysis. II - Nonlinear evolution*, apj, 376 (1991), pp. 214–233.

[5] J. A. BALDWIN, M. M. PHILLIPS, AND R. TERLEVICH, *Classification parameters for the emission-line spectra of extragalactic objects*, pasp, 93 (1981), pp. 5–19.

[6] P. D. BARTHEL, *Unified Schemes of FR2 Radio Galaxies and Quasars*, in The Physics of Active Galaxies, G. V. Bicknell, M. A. Dopita, and P. J. Quinn, eds., vol. 54 of Astronomical Society of the Pacific Conference Series, 1994, p. 175.

[7] T. S. BERGMANN, *Resolved Outflows in Nearby AGN from Integral Field Spectroscopy*, in AGN Winds in Charleston, G. Chartas, F. Hamann, and K. M. Leighly, eds., vol. 460 of Astronomical Society of the Pacific Conference Series, Aug. 2012, p. 133.

[8] F. BERTOLA, D. BETTONI, J. DANZIGER, E. SADLER, L. SPARKE, AND T. DE ZEEUW, *Testing the gravitational field in elliptical galaxies - NGC 5077*, apj, 373 (1991), pp. 369–390.

[9] P. N. BEST AND T. M. HECKMAN, *On the fundamental dichotomy in the local radio-AGN population: accretion, evolution and host galaxy properties*, mnras, 421 (2012), pp. 1569–1582.

[10] J. BINNEY AND S. TREMAINE, *Galactic Dynamics: Second Edition*, Princeton University Press, 2008.

[11] R. D. BLANDFORD AND D. G. PAYNE, *Hydromagnetic flows from accretion discs and the production of radio jets*, mnras, 199 (1982), pp. 883–903.

[12] M. CAPPELLARI, *Improving the full spectrum fitting method: accurate convolution with Gauss-Hermite functions*, mnras, 466 (2017), pp. 798–811.

[13] M. CAPPELLARI AND Y. COPIN, *Adaptive spatial binning of integral-field spectroscopic data using Voronoi tessellations*, mnras, 342 (2003), pp. 345–354.

[14] M. CAPPELLARI AND E. EMSELLEM, *Parametric Recovery of Line-of-Sight Velocity Distributions from Absorption-Line Spectra of Galaxies via Penalized Likelihood*, pasp, 116 (2004), pp. 138–147.

[15] S. M. CHUNG, C. S. KOCHANEK, R. ASSEF, M. J. I. BROWN, D. STERN, B. T. JANNUZI, A. H. GONZALEZ, R. C. HICKOX, AND J. MOUSTAKAS, *A UV to Mid-IR Study of AGN Selection*, apj, 790 (2014), p. 54.

[16] G. D. S. COUTO, T. STORCHI-BERGMANN, R. A. RIFFEL, D. J. AXON, AND A. ROBINSON, *GMOS IFU Observations of the Gas Kinematics in the Radio Galaxy Arp 102B*, in Co-Evolution of Central Black Holes and Galaxies, B. M. Peterson, R. S. Somerville, and T. Storchi-Bergmann, eds., vol. 267 of IAU Symposium, May 2010, pp. 395–395.

[17] G. S. COUTO, T. STORCHI-BERGMANN, D. J. AXON, A. ROBINSON, P. KHARB, AND R. A. RIFFEL, *Kinematics and excitation of the nuclear*

spiral in the active galaxy Arp 102B, in Revista Mexicana de Astronomia y Astrofisica Conference Series, vol. 44 of Revista Mexicana de Astronomia y Astrofisica Conference Series, Oct. 2014, pp. 191–192.

[18] D. M. CRENSHAW AND S. B. KRAEMER, *Feedback from Mass Outflows in Nearby Active Galactic Nuclei. I. Ultraviolet and X-Ray Absorbers*, apj, 753 (2012), p. 75.

[19] A. C. CROOK, J. P. HUCHRA, N. MARTIMBEAU, K. L. MASTERS, T. JARRETT, AND L. M. MACRI, *Groups of Galaxies in the Two Micron All Sky Redshift Survey*, apj, 655 (2007), pp. 790–813.

[20] R. I. DAVIES, W. MACIEJEWSKI, E. K. S. HICKS, L. J. TACCONI, R. GENZEL, AND H. ENGEL, *Stellar and Molecular Gas Kinematics Of NGC 1097: Inflow Driven by a Nuclear Spiral*, apj, 702 (2009), pp. 114–128.

[21] M. H. K. DE GRIJP, W. C. KEEL, G. K. MILEY, P. GOUDFROOIJ, AND J. LUB, *Warm IRAS sources. II - Optical spectroscopy of objects from the point source catalog*, aaps, 96 (1992), pp. 389–428.

[22] M. H. DEMOULIN AND E. M. BURBIDGE, *Noncircular Gas Motions in NGC 253: Evidence for Outflow from the Center*, apj, 159 (1970), p. 799.

[23] G. DUMAS, C. G. MUNDELL, E. EMSELLEM, AND N. M. NAGAR, *Central kiloparsec of Seyfert and inactive host galaxies: a comparison of two-dimensional stellar and gaseous kinematics*, mnras, 379 (2007), pp. 1249–1278.

[24] S. M. FABER AND J. S. GALLAGHER, *Masses and mass-to-light ratios of galaxies*, araa, 17 (1979), pp. 135–187.

[25] M. A. GALLOWAY, K. W. WILLETT, L. F. FORTSON, C. N. CARDAMONE, K. SCHAWINSKI, E. CHEUNG, C. J. LINTOTT, K. L. MASTERS, T. MELVIN, AND B. D. SIMMONS, *Galaxy Zoo: the effect of bar-driven fuelling on the presence of an active galactic nucleus in disc galaxies*, mnras, 448 (2015), pp. 3442–3454.

[26] C. M. GASKELL AND R. W. GOOSMANN, *Line Shifts, Broad-line Region Inflow, and the Feeding of Active Galactic Nuclei*, apj, 769 (2013), p. 30.

[27] J. M. GELBORD, J. R. MULLANEY, AND M. J. WARD, *AGN with strong forbidden high-ionization lines selected from the Sloan Digital Sky Survey*, mnras, 397 (2009), pp. 172–189.

[28] G. GIURICIN, M. MEZZETTI, AND F. MARDIROSSIAN, *A search for environmental effects on the optical properties of galaxies in groups*, aaps, 62 (1985), pp. 157–172.

[29] J. W. GOAD, S. E. STROM, AND L. E. GOAD, *NGC 5364 and the Density-Wave Model*, in Bulletin of the American Astronomical Society, vol. 7 of baas, June 1975, p. 395.

[30] T. GOTO, *Post-starburst-active galactic nucleus connection: spatially resolved spectroscopy of Hδ-strong active galactic nuclei*, mnras, 369 (2006), pp. 1765–1772.

[31] C. A. HEISLER AND M. M. DE ROBERTIS, *A Near-Infrared Spectroscopic Study of 60 Micron Peakers*, aj, 118 (1999), pp. 2038–2054.

[32] C. A. HEISLER AND J. P. VADER, *Galaxies with spectral energy distributions peaking near 60 microns. 2: Optical broadband properties*, aj, 107 (1994), pp. 35–66.

[33] ——, *Galaxies with Spectral Energy Distributions Peaking Near 60 micron.III. H(alpha) Imaging*, aj, 110 (1995), p. 87.

[34] P. W. HODGE, *H II regions in galaxies*, pasp, 86 (1974), pp. 845–860.

[35] J. P. HUCHRA, M. S. VOGELEY, AND M. J. GELLER, *The CFA Redshift Survey: Data for the South Galactic CAP*, apjs, 121 (1999), pp. 287–368.

[36] W. K. HUCHTMEIER, *Rotation-curves of galaxies from 21 cm-line observations*, aap, 45 (1975), pp. 259–268.

[37] P. A. JAMES, N. S. SHANE, J. H. KNAPEN, J. ETHERTON, AND S. M. PERCIVAL, *The Hα Galaxy Survey. II. Extinction and [NII] corrections to Hα fluxes*, aap, 429 (2005), pp. 851–867.

[38] A. L. KINNEY, H. R. SCHMITT, C. J. CLARKE, J. E. PRINGLE, J. S. ULVESTAD, AND R. R. J. ANTONUCCI, *Jet Directions in Seyfert Galaxies*, apj, 537 (2000), pp. 152–177.

[39] S. B. KRAEMER, D. M. CRENSHAW, J. P. DUNN, T. J. TURNER, A. P. LOBBAN, L. MILLER, J. N. REEVES, T. C. FISCHER, AND V. BRAITO, *Observations of Outflowing Ultraviolet Absorbers in NGC 4051 with the Cosmic Origins Spectrograph*, apj, 751 (2012), p. 84.

[40] R. LARSON, *Inflows and Outbursts in Galaxies*, in Mass-Transfer Induced Activity in Galaxies, I. Shlosman, ed., 1994, p. 489.

[41] D. LENA, A. ROBINSON, T. STORCHI-BERGMAN, A. SCHNORR-MÜLLER, T. SEELIG, R. A. RIFFEL, N. M. NAGAR, G. S. COUTO, AND L. SHADLER, *The Complex Gas Kinematics in the Nucleus of the Seyfert 2 Galaxy NGC 1386: Rotation, Outflows, and Inflows*, apj, 806 (2015), p. 84.

[42] A. MAHDAVI AND M. J. GELLER, *A Redshift Survey of Nearby Galaxy Groups: The Shape of the Mass Density Profile*, apj, 607 (2004), pp. 202–219.

[43] P. MARTINI AND R. W. POGGE, *Hubble Space Telescope Observations of the CFA Seyfert 2 Galaxies: The Fueling of Active Galactic Nuclei*, aj, 118 (1999), pp. 2646–2657.

[44] D. MERRITT AND L. FERRARESE, *The M-σ Relation for Supermassive Black Holes*, apj, 547 (2001), pp. 140–145.

[45] D. C. MORTON AND C. D. ANDERECK, *The H and K lines of CA II in the nucleus and bulge of M31*, apj, 205 (1976), pp. 356–359.

[46] A. S. MÜLLER, T. STORCHI-BERGMANN, AND N. M. NAGAR, *Mapping NGC 2110 Nuclear Outflows with GMOS-IFU*, in AGN Winds in Charleston, G. Chartas, F. Hamann, and K. M. Leighly, eds., vol. 460 of Astronomical Society of the Pacific Conference Series, Aug. 2012, p. 167.

[47] P. B. NAIR AND R. G. ABRAHAM, *A Catalog of Detailed Visual Morphological Classifications for 14,034 Galaxies in the Sloan Digital Sky Survey*, apjs, 186 (2010), pp. 427–456.

[48] D. E. OSTERBROCK, *Astrophysics of gaseous nebulae and active galactic nuclei*, 1989.

[49] D. E. OSTERBROCK AND G. J. FERLAND, *Astrophysics of gaseous nebulae and active galactic nuclei*, 2006.

[50] G. PATUREL, C. PETIT, P. PRUGNIEL, G. THEUREAU, J. ROUSSEAU, M. BROUTY, P. DUBOIS, AND L. CAMBRÉSY, *HYPERLEDA. I. Identification and designation of galaxies*, aap, 412 (2003), pp. 45–55.

[51] F. G. PEASE, *The Spiral Nebula Messier 33*, pasp, 28 (1916), p. 33.

[52] ——, *The rotation and radial velocity of the spiral nebula N. G. C. 4594*, in Publications of the American Astronomical Society, vol. 3 of Publications of the American Astronomical Society, 1918, p. 213.

[53] A. PELLET, *Rotation in the central region of M 31*, aap, 50 (1976), pp. 421–428.

[54] E. A. PIER AND J. H. KROLIK, *Infrared Spectra of Obscuring Dust Tori around Active Galactic Nuclei. II. Comparison with Observations*, apj, 418 (1993), p. 673.

[55] M. A. PRIETO, W. MACIEJEWSKI, AND J. REUNANEN, *Feeding the Monster: The Nucleus of NGC 1097 at Subarcsecond Scales in the Infrared with the Very Large Telescope*, aj, 130 (2005), pp. 1472–1481.

[56] R. A. RIFFEL, *profit: a new alternative for emission-line profile fitting*, apss, 327 (2010), pp. 239–244.

[57] R. A. RIFFEL AND T. STORCHI-BERGMANN, *Compact molecular disc and ionized gas outflows within 350 pc of the active nucleus of Mrk 1066*, mnras, 411 (2011), pp. 469–486.

[58] M. S. ROBERTS AND A. H. ROTS, *Comparison of Rotation Curves of Different Galaxy Types*, aap, 26 (1973), pp. 483–485.

[59] M. S. ROBERTS AND R. N. WHITEHURST, *The rotation curve and geometry of M31 at large galactocentric distances.*, apj, 201 (1975), pp. 327–346.

[60] V. C. RUBIN AND W. K. FORD, JR., *Radial Velocities and Line Strengths of Emission Lines across the Nuclear Disk of M31*, apj, 170 (1971), p. 25.

[61] V. C. RUBIN, W. K. FORD, JR., AND C. KRISHNA KUMAR, *Stellar Motions Near the Nucleus of M31*, apj, 181 (1973), pp. 61–78.

[62] V. C. RUBIN, C. J. PETERSON, AND W. K. FORD, JR., *Evidence for contraction in the nuclear ring of the barred spiral galaxy NGC 3351*, apj, 199 (1975), pp. 39–41.

[63] P. SÁNCHEZ-BLÁZQUEZ, R. F. PELETIER, J. JIMÉNEZ-VICENTE, N. CARDIEL, A. J. CENARRO, J. FALCÓN-BARROSO, J. GORGAS, S. SELAM, AND A. VAZDEKIS, *Medium-resolution Isaac Newton Telescope library of empirical spectra*, mnras, 371 (2006), pp. 703–718.

[64] H. R. SCHMITT, J. L. DONLEY, R. R. J. ANTONUCCI, J. B. HUTCHINGS, A. L. KINNEY, AND J. E. PRINGLE, *A Hubble Space Telescope Survey of Extended [O III] λ5007 Å Emission in a Far-Infrared-Selected Sample of Seyfert Galaxies: Results*, apj, 597 (2003), pp. 768–779.

[65] H. R. SCHMITT AND A. L. KINNEY, *Jet Directions in Seyfert Galaxies: B and I Imaging Data*, apjs, 128 (2000), pp. 479–489.

[66] H. R. SCHMITT, J. S. ULVESTAD, R. R. J. ANTONUCCI, AND A. L. KINNEY, *Jet Directions in Seyfert Galaxies: Radio Continuum Imaging Data*, apjs, 132 (2001), pp. 199–209.

[67] A. SCHNORR-MÜLLER, T. STORCHI-BERGMANN, N. M. NAGAR, AND F. FERRARI, *Gas inflows towards the nucleus of the active galaxy NGC 7213*, mnras, 438 (2014), pp. 3322–3331.

[68] A. SCHNORR-MÜLLER, T. STORCHI-BERGMANN, N. M. NAGAR, A. ROBINSON, D. LENA, R. A. RIFFEL, AND G. S. COUTO, *Feeding and feedback in the inner kiloparsec of the active galaxy NGC 2110*, mnras, 437 (2014), pp. 1708–1724.

[69] C. K. SEYFERT, *Nuclear Emission in Spiral Nebulae.*, apj, 97 (1943), p. 28.

[70] N. I. SHAKURA AND R. A. SUNYAEV, *Black holes in binary systems. Observational appearance.*, aap, 24 (1973), pp. 337–355.

[71] F. H. SHU, *Density-Wave Theory of Spiral Structure*, in NATO Advanced Science Institutes (ASI) Series C, K. Pinkau, ed., vol. 6 of NATO Advanced Science Institutes (ASI) Series C, 1974, p. 219.

[72] S. M. SIMKIN, *Observational Evidence for Inward Radial Streaming in Two Spiral Galaxies.*, in Bulletin of the American Astronomical Society, vol. 6 of baas, June 1974, p. 321.

[73] T. STORCHI-BERGMANN, *Inflows and Outflows in Nearby AGN from Integral Field Spectroscopy*, in Co-Evolution of Central Black Holes and Galaxies, B. M. Peterson, R. S. Somerville, and T. Storchi-Bergmann, eds., vol. 267 of IAU Symposium, May 2010, pp. 290–298.

[74] T. STORCHI-BERGMANN, O. L. DORS, JR., R. A. RIFFEL, K. FATHI, D. J. AXON, A. ROBINSON, A. MARCONI, AND G. ÖSTLIN, *Nuclear Spirals as Feeding Channels to the Supermassive Black Hole: The Case of the Galaxy NGC 6951*, apj, 670 (2007), pp. 959–967.

[75] Y. TOBA, S. OYABU, H. MATSUHARA, M. A. MALKAN, D. ISHIHARA, T. WADA, Y. OHYAMA, S. TAKITA, AND C. YAMAUCHI, *The 9 and 18 Micrometer Luminosity Functions of Various Types of Galaxies with AKARI: Implication for the Dust Torus Structure of AGN*, pasj, 65 (2013), p. 113.

[76] D. TOYOUCHI AND M. CHIBA, *Gas Inflow and Outflow Histories in Disk Galaxies as Revealed from Observations of Distant Star-forming Galaxies*, apj, 810 (2015), p. 18.

[77] M.-H. ULRICH, *Observations of the outflow of gas from the nucleus of NGC 253 and its implications for the stellar population of the nucleus*, apj, 219 (1978), pp. 424–436.

[78] S. W. UNGER, A. PEDLAR, D. J. AXON, M. WHITTLE, E. J. A. MEURS, AND M. J. WARD, *The extended narrow-line region in radio Seyferts - Evidence for a collimated nuclear UV field?*, mnras, 228 (1987), pp. 671–679.

[79] C. M. URRY AND P. PADOVANI, *Unified Schemes for Radio-Loud Active Galactic Nuclei*, pasp, 107 (1995), p. 803.

[80] ——, *The Unification of Radio-Loud AGN*, in Extragalactic Radio Sources, R. D. Ekers, C. Fanti, and L. Padrielli, eds., vol. 175 of IAU Symposium, 1996, p. 379.

[81] P. C. VAN DER KRUIT, *The motions in the central region of NGC 4736: Evidence for an expanding ring.*, apj, 188 (1974), pp. 3–17.

[82] ——, *The velocity field in the inner part of NGC 4736.*, aap, 52 (1976), pp. 85–92.

[83] P. C. VAN DER KRUIT AND R. J. ALLEN, *The kinematics of spiral and irregular galaxies*, araa, 16 (1978), pp. 103–139.

[84] P. J. WARNER, M. C. H. WRIGHT, AND J. E. BALDWIN, *High resolution observations of neutral hydrogen in M33 - II. The velocity field.*, mnras, 163 (1973), pp. 163–182.

[85] M. WHITTLE, A. PEDLAR, E. J. A. MEURS, S. W. UNGER, D. J. AXON, AND M. J. WARD, *Radio lobes and forbidden O III profile substructure in Seyfert galaxies*, apj, 326 (1988), pp. 125–145.

[86] L. WOLTJER, *Emission Nuclei in Galaxies.*, apj, 130 (1959), p. 38.

[87] A. V. ZASOV, A. V. MOISEEV, A. V. KHOPERSKOV, AND E. A. SIDOROVA, *Early-type disk galaxies: Structure and kinematics*, Astronomy Reports, 52 (2008), pp. 79–93.